

THE UNIVERSITY OF MICHIGAN PROGRAM IN SHIP HYDRODYNAMICS



COLLEGE OF ENGINEERING

NAVAL ARCHITECTURE &
MARINE ENGINEERING

AEROSPACE ENGINEERING

MECHANICAL ENGINEERING &
APPLIED MECHANICS

SHIP HYDRODYNAMIC
LABORATORY

SPACE PHYSICS RESEARCH
LABORATORY



AD-A251 102



①

DTIC

ELECTE

JUN 1 1992

S

C

D

**Potential Energy in Steep
and Breaking Waves**

W. W. Schultz

Department of Mechanical Engineering and Applied Mechanics
University of Michigan, Ann Arbor, Michigan 48109-2125

O.M. Griffin

Laboratory for Computational Physics and Fluid Dynamics
Naval Research Laboratory, Washington, DC 20375-5000

S.E. Ramberg

Ocean Engineering Division
Office of Naval Research, Arlington, Virginia 22217-5000

Contract Number N00014-86-K-0684

Technical Report No. 89-10

December 13, 1989

DISTRIBUTION STATEMENT A

Approved for public release;
Distribution Unlimited

92-13801



92 5 26 0217

NWW 6/1/92

Accession For	
ONR/Code	<input checked="" type="checkbox"/>
Dist	<input type="checkbox"/>
Availability	<input type="checkbox"/>
Justification	
By	
Distribution	
Availability Codes	
Dist	Avail and/or Special
A-1	

Abstract

We find that potential energy rather than wave height is a better experimental and analytic criterion for determining when wave breaking will occur. A simple two-dimensional, periodic algorithm is developed and used to compare breaking onset criteria for energy input from (1) converging sidewalls, (2) a submerged disturbance and (3) wave focusing. Wave-breaking criteria (potential energy or the more classical peak-to-peak wave height) are a function of the rate of energy input. Large plunging waves occur for large energy input rates with a smooth transition to smaller spilling waves for lesser energy input rates. The first two kinds of energy input show similar trends in the limit as the energy input rate becomes small. The third case, wave focusing, is the subject of an ongoing investigation. The effects of wave modulation and reflection are also discussed.



1 Introduction

The overall morphology of the surface hydrodynamics of ship wakes is strongly affected by breaking waves, especially at the bow and in the near wake. There are essentially two types of breaking waves—plunging breakers (with a large degree of overturning) and spilling breakers (with white water only near the crest). Plunging breakers are an important factor in the overturning of ships in rough seas, and they often form continuously at the bow, producing bubbles and foam that strongly affect the signature of a ship wake. Spilling breakers are more common in the open ocean (due to wind) and in breaking wave experiments; they also occur in the near-ship Kelvin wave pattern.

A recent discussion of ship wake hydrodynamics and the related remote sensing issues is given by Griffin et al. (1989) and extensive summaries of breaking waves are available (Cokelet, 1978; Kjeldsen and Myrhaug, 1978; Griffin, 1984). While

the mechanisms for plunging and spilling breaking waves are often thought to be quite different, we will show that their formation is similar with their qualitative features depending mainly on the energy input rate.

The fundamental experiments for determining two-dimensional wave-breaking criteria (apart from that induced by wind-wave interaction) fall into three main categories: (1) the focusing of essentially two-dimensional waves in the lateral direction (Ramberg and Griffin, 1987; Van Dorn and Pazan, 1975); (2) the towing of a submerged object such as a hydrofoil (Duncan, 1981, 1983); and (3) the focusing of variable length waves from a modulated wavemaker or wave source (Dommermuth et al., 1988; Duncan et al., 1987). These experimental studies propose a wave-breaking criterion based on the peak-to-peak (crest-to-trough) wave heights.

However, the validity of this standard criterion has been questioned (Melville and Rapp, 1988), in part because peak-to-peak wave heights vary significantly during breaking and often decrease just before breaking. Any criterion will be complicated since wave breaking is not amenable to analysis, and experimentally or computationally determined criteria will be a function of many parameters. Extensive discussions of breaking criteria based on wave height are given in Ochi and Tsai (1983) and Huang et al. (1986). Breaking criteria based upon crest acceleration are discussed by Srokosz (1986) and Longuet-Higgins (1985). An experimental determination of the onset of breaking is also difficult without detailed velocity measurements at the crest (Melville and Rapp, 1988; Van Dorn and Pazan, 1975), which are usually not available and are difficult to obtain.

Computational studies of breaking waves usually apply a point pressure distur-

bance (Longuet-Higgins and Cokelet, 1976) or obtain breaking conditions simply from having energetic initial conditions (Vinje and Brevig, 1981). While many new algorithms have been developed for breaking waves, no study has systematically examined the parameters that cause wave breaking. For example, wave breaking caused by a modulated wavemaker has been verified by computations (Dommermuth, et al., 1988), but these were so expensive that only one experimental event was verified. In addition, previous computations tend to show plunging waves instead of the more commonly observed spilling breakers.

In this study, we computationally examine the steepening and breaking of deep water waves generated by the experimental methods cited above. We consider only spatially periodic computations, so an *ad hoc* energy input term is deduced for the convergent wave channel. Although the periodic boundary conditions preclude studying the wavemaker problem, we briefly examine the effect of wave modulation by examining a larger computational region (more than one primary wavelength) as in Dold and Peregrine (1986). The effect of reflection from a beach can be considered by putting a small standing wave component in the initial conditions. Finally, to compare to the second type of experiment we use an array of submerged disturbances (dipoles in this case) to preserve spatial periodicity.

There are difficulties in interpreting the differences caused by the computational spatial periodicity as compared to temporal periodicity (for the unmodulated wavemaker) of the experiments. This also affects comparisons of temporal vs. spatial growth when we model a convergent channel. Also, experiments continue after breaking occurs, while the time-marching computations must stop at the first oc-

currence of breaking unless an *ad hoc* condition is used to model the turbulence and air entrainment. There is evidence that accurate spectral computations break down sooner (Huh and Schultz, 1989), indicating the possible formation of a singularity and the failure of potential theory before the wave crest approaches the forward face.

In this report, experimental data for the wave height only are analyzed since these are the traditional measurements and are easily obtained compared to velocity measurements. This data is used to show that the potential energy reduces the experimental scatter in breaking criteria and to show it acts as a better *predictor* (rather than just indicator) of breaking.

In section 2, we pose the problem for periodic waves, including the modelling of the growth in energy and the effect of submerged disturbances. Section 3 contains a summary of earlier computational progress followed by a formulation of the two computational techniques used in this study. Section 4 presents numerical results, including comparisons to related computational schemes and the development of breaking criteria as a function of the energy input rate. The computations are compared to previous experiments in section 5. Measurements of momentum and energy losses after breaking are presented in section 6, and section 7 summarizes the findings.

2 Problem Formulation

The problem domain is shown in Fig. 1. The scales are chosen to make gravity and the primary wavenumber unity. The phase speed and angular velocity of a linear wave will then be unity as well. The initial boundary value problem solution is described by a complex potential $w(\xi) = \phi + i\psi$, where ϕ is the velocity potential, ψ is the stream function and $\xi = x + iy$ represents the two spatial coordinates. At every time step, the unknown boundary values of the velocity potential (half of the values are known from the boundary conditions) are solved using the Cauchy integral theorem:

$$\oint_{\partial\Omega} \frac{w(\xi)}{\xi - \zeta_k} d\xi = i\alpha w(\zeta_k), \quad (1)$$

where α is 0 or 2π if the location of the kernel singularity, ζ_k , is outside or inside the boundary, respectively. If the kernel singularity is on the boundary ($\zeta_k \in \partial\Omega$), α is equal to the included angle, and the integral is treated as principal-valued.

The kinematic and dynamic boundary conditions of a free surface for an inviscid flow are given as

$$\frac{D\xi}{Dt} = \frac{dw^*}{d\xi} \quad (2)$$

and

$$\frac{D\phi}{Dt} = -y + \frac{1}{2} \left| \frac{dw^*}{d\xi} \right|^2 - p. \quad (3)$$

Here, p is a prescribed pressure (normally 0, as in this study, unless surface tension or wind effects are included), D/Dt is a material derivative, and $*$ denotes the complex conjugate. The kinematic condition requires that material particles on the free surface stay on the free surface, and the dynamic boundary condition

requires that the pressure remains constant at the free surface in the absence of surface tension.

We complete the problem by applying a periodic boundary condition in the horizontal direction, $w(\xi) = w(\xi + 2\pi)$, the deep water condition requiring $w \rightarrow 0$ as $y \rightarrow -\infty$, and initial conditions. These initial conditions on the free surface can be homogeneous if the waves are forced by submerged dipoles. For purposes of illustration and comparison, we generally use the same initial conditions as McIver and Peregrine (1981):

$$\eta = a \sin x \quad \text{and} \quad \phi = a \cos x. \quad (4)$$

These initial conditions satisfy linear theory as the wave amplitude a approaches 0. We apply increasing values of a until the wave breaks. We also apply more complicated initial conditions to examine wave modulation and the effect of applying initial conditions computed from steadily progressing waveforms using the method of Schwartz and Vanden-Broeck (1979).

2.1 Modelling the convergent wave channel

The convergent channel is inherently a three-dimensional problem. If the convergence is small in z , the spanwise direction out of the plane of Fig. 1, a multiple-scales approach will lead to the three-dimensional effect being delayed to a Poisson equation at higher order, with the lowest-order solution being that of a non-convergent wave channel. The sidewall boundary condition simply becomes $\phi_z = \epsilon \phi_x$, where ϵ is the slope of the converging walls and the subscripts x and z rep-

resent partial differentiation. This method of analysis precludes the possibility of modelling the flow as spatially periodic and hence makes the problem intractable using periodic algorithms.

If instead we model the channel as one with straight walls converging in time, we can continue to model the problem as spatially periodic. We assume that the convergent channel sidewall boundary conditions can be approximated by

$$\phi_z = \pm \epsilon c_g \quad \text{at } z = z_w = z_o \pm \epsilon c_g t, \quad (5)$$

where z_o is the scaled width of the channel at the wavemaker and c_g is the average group velocity of the fundamental wave. These conditions lead to a two-dimensional Poisson equation with a small right-hand side:

$$\phi_{xx} + \phi_{yy} = - \frac{\epsilon c_g}{z_o - \epsilon c_g t}. \quad (6)$$

This assumption is not satisfactory because it requires significant flow at infinite depths and consequently the Poisson equation cannot be made into the easily computed Laplace equation.

Instead of using the multiple-scales approach or allowing the sidewalls to converge in time, we simply add a term in the Bernoulli equation that causes the energy to increase exponentially in time so that (3) becomes

$$\frac{D\phi}{Dt} = -y + \frac{1}{2} \left| \frac{dw^*}{d\xi} \right|^2 + \gamma \phi. \quad (7)$$

This is similar (but with the opposite sign) to the dissipative effect used by Lamb to develop the radiation condition. Starting with a wave of small amplitude, this term eventually causes the wave to break, much like the convergent channel. While this

causes exponential temporal growth in the computations, the experimental energy per unit width, E , grows in space. The corresponding temporal growth parameter can be approximately related through the group velocity and conservation of energy by

$$\gamma = \frac{1}{E} \frac{dE}{dt} = -\frac{1}{z_w} \frac{dz_w}{dt} = -\frac{1}{z_w} \frac{dz_w}{dx} c_g = \frac{\epsilon c_g}{z_w}. \quad (8)$$

The dimensionless values ($\epsilon = 1/16$) for the experiments considered here correspond to

$$\gamma = K \frac{T^2}{W}, \quad (9)$$

where the dimensional constant K is $.008\text{m/s}^2$, and W and T are the dimensional values of the local channel width and wavemaker period, respectively. This keeps the growth parameter below 0.05 in the region of breaking.

2.2 Modelling periodic submerged disturbances

We wish to show how submerged disturbances can force wave breaking because this case is far easier to compute accurately than surface-piercing bodies. To keep the periodic boundary condition requires that the disturbances be periodic. Rather than modelling a complex two-dimensional shape such as a hydrofoil, we use a periodic array of moving dipoles:

$$w_{dp} = a_{dp} \cot\left[\frac{1}{2}(\xi - \xi_{dp})\right], \quad (10)$$

where a_{dp} and ξ_{dp} are the strength and location of the dipole, respectively. The dipole depth, d_{dp} , and velocity, v_{dp} , are prescribed such that $\xi_{dp} = (v_{dp}t, -d_{dp})$. As

long as the strength of the dipole is not too large and the depth is not too small, the dipole can closely represent a cylinder of radius r_{dp} if $a_{dp} = v_{dp} r_{dp}^2 / 2$.

Since the dipole represents a simple pole in the complex potential plane, the only alteration required is to subtract out the singular part and solve only for the remaining regular term from the integral equation (1).

3 Computations of Steep and Breaking Waves

3.1 Recent computational advances

Although formal analytical techniques have been developed for small-amplitude gravity waves, unsteady and steep waves must be solved numerically. The most efficient of these algorithms are based on boundary integral techniques. Even then, the algorithms can be rather time consuming. Hence, no thorough and complete parametric study has been performed on gravity waves. Even more important, to reduce the computational effort, the problem domain is kept as small as possible by applying periodic boundary conditions. Recently, computations with many fundamental wavelengths inside the periodic domain have been applied by Dold and Peregrine (1986), and the nonperiodic fully nonlinear wavemaker problem has been computed by Dommermuth et al. (1988). Casual observations of breaking waves show that they are not spatially periodic. In this report, we only present results for the periodic problem, although by using a large spatial period, the model can represent results on an infinite domain.

The boundary integral numerical schemes for irrotational flow problems can be

broken into three general approaches based on Green's functions (Longuet-Higgins and Cokelet, 1976; Vanden-Broeck, 1980), vortex dynamics (Baker, Meiron and Orszag, 1982), or the Cauchy integral theorem for complex potentials (Vinje and Brevig, 1981). To some extent, the three techniques give equivalent results (McIver and Peregrine, 1981). Recent work (Dold and Peregrine, 1984) has shown that algorithms based on the Cauchy Integral theorem can be up to 50 times faster than Green's function algorithms and 10 times faster than those using vortex methods. Lin et al. (1984) use the Cauchy formulation when solving two-dimensional problems and revert to the Green's function algorithm for axisymmetric problems. Apparently, the efficiency of the complex algebra is significant and normal derivatives of the Green's function need not be found.

Here we report on two algorithms based on the Cauchy integral theorem. The first is an improvement of a piecewise-linear algorithm of Vinje and Brevig (1981) as described in Schultz and Hong (1989). The second is a spectral technique similar to that proposed by Roberts (1983) and described in Huh and Schultz (1989). We describe both methods because the first method, although less accurate and more computationally intensive, is also more robust. Comparisons will be presented.

In both methods, the physical domain is mapped to an approximate unit circle using the conformal transformation:

$$\zeta = e^{iz} \quad (11)$$

(see Fig. 1). This eliminates the periodic boundary conditions and sharp computational corners used by Vinje and Brevig (1981). All derivatives are taken in the conformed space—the piecewise-linear method uses three-point central differences

while the spectral method takes derivatives in the spectral space of the conformed representation. An alternate method (not used here) does not use conformal mapping but replaces the infinitely periodic integrand with a summation over a finite domain to form a cotangent kernel, as in Baker et al. (1982).

The algebraic system that results from discretizing the integral equation is iteratively solved for both methods using a generalized minimum residual method (GMRES) based on the work of Saad and Schultz (1986). This variation of the conjugate gradient method for nonsymmetric matrices works very well on the diagonally dominant matrices of either method—especially the matrices from the spectral algorithm. The time marching is also similar in both algorithms. Fourth-order Runge-Kutta-Gill and Hamming predictor-corrector methods with an automatic adjustment of step size were both used, with the predictor-corrector method showing the greater computational efficiency, especially for the higher-accuracy computations. Filtering of the spectral computations is probably necessary to allow them to proceed closer to breaking, although none was performed here. Filtering is discussed in Huh and Schultz (1989).

3.2 Piecewise-linear computational technique

We take ζ_k in (1) to approach the boundary from the outside of the domain so that α is zero, although there are computational reasons for placing ζ_k slightly away from the contour in some cases (Schultz and Hong, 1989). The algebraic system is formed by discretization of (1), as explained in Vinje and Brevig (1981), and by letting the kernel singularity approach each of the N nodal points, i.e., $\zeta_k \rightarrow \xi_k$. A

special limiting process is needed to evaluate the integration near ζ_k . The system of linear algebraic equations when w is discretized as a piecewise-linear function between the N boundary nodes is as follows:

$$\sum_{j=1}^N w_j \Gamma_{jk} = 0 \quad \text{for } k = 1, \dots, N \quad (12)$$

where

$$\Gamma_{jk} = \frac{\xi_{j+1} - \zeta_k}{\xi_{j+1} - \xi_j} \ln\left(\frac{\xi_{j+1} - \zeta_k}{\xi_j - \zeta_k}\right) - \frac{\xi_{j-1} - \zeta_k}{\xi_j - \xi_{j-1}} \ln\left(\frac{\xi_j - \zeta_k}{\xi_{j-1} - \zeta_k}\right) \quad \text{for } j \neq k, \quad (13)$$

$$\Gamma_{kk} = \ln\left(\frac{\xi_{k+1} - \xi_k}{\xi_{k-1} - \xi_k}\right). \quad (14)$$

Eq. (13) is evaluated using l'Hopital's rule when $j = k + 1$ or $k - 1$. Moving the known boundary conditions to the right-hand side gives a complex algebraic system for unknown ψ_j on the free surface.

When the complex potential is known along the domain boundary, the solution can be stepped forward in time using the Bernoulli equation and the kinematic boundary conditions. We solve this problem in a similar way to Vinje and Brevig with (1981) the following changes:

- 1) Rather than using the real or imaginary parts of the discretized Cauchy integral theorem (depending on whether the real or imaginary part of w is known), we use both to give $2N$ real equations and N real unknowns. Numerical experiments for known test cases (Schultz and Hong, 1989) show that the least-squares solution is better for nearly circular contours, especially when the node placement is irregular (as will be the case after nodes are convected on the free surface); however, both results are second-order convergent. The solution time for a direct method of inverting the overdetermined system would be twice that of the determined system

but our experience with iterative conjugate gradient solvers indicates an increase in computational costs of only 10 percent.

2) We use a conformal map to eliminate the bottom and periodic boundary conditions.

3) We use a central difference form for $dw/d\xi$ (or $dw/d\zeta$), while Vinje and Brevig use a truncated analytic form. Since the solution is piecewise-linear rather than analytic, we have found that some numerical instabilities can develop using the truncated analytic form. One can easily find examples where the derivative $dw/d\xi$ at a corner of the contour computed using the analytic form lies outside the range computed by the forward and backward derivatives. This violates the spirit of using piecewise-linear functions and can lead to numerical instabilities, although the truncated analytic form works better when the contour is smooth.

3.3 Spectral computational technique

Roberts (1983) used a desingularized kernel in his vortex formulation. Generally, it is difficult to find a suitable desingularized form of a kernel in an integral equation, but in the complex formulation it is relatively simple. The Cauchy integral equation (3) can easily be rewritten as

$$\oint \frac{w(s) - w(\zeta_k) \frac{d\xi}{ds}}{\xi(s) - \zeta_k} ds = 0, \quad (15)$$

where the principal value integral can be replaced by the closed contour integral since the integrand is no longer singular. When ξ approaches ζ_k , the integrand approaches dw/ds at the k th node point. Therefore, this kernel does not show the

singular behavior as ξ approaches ξ_k . The integral equation (1) is converted to the following sets of equations for $k = 1 \dots N$:

$$\sum_{j=1}^N I_{jk} = 0 \quad \text{for } k = 1, \dots, N, \quad (16)$$

where N is the number of nodes, and I_{jk} is represented by

$$I_{jk} = \begin{cases} \frac{w_j - w_k}{\xi_j - \xi_k} \left(\frac{dw}{ds} \right)_j & \text{if } j \neq k \\ \left(\frac{dw}{ds} \right)_k & \text{if } j = k. \end{cases} \quad (17)$$

The algebraic system (7) effectively becomes a differential system because I_{jk} includes the derivative of w . To evaluate these derivatives spectrally, we use a cardinal function representation of w (Boyd, 1989):

$$w(s) = \sum_{j=1}^N C_j(s) w_j, \quad (18)$$

where

$$C_j = \frac{1}{N} \sin \pi(s - s_j) \cot \frac{\pi}{N}(s - s_j), \quad (19)$$

and the derivative of C_j is

$$\frac{dC_j}{ds}(s_i) = \begin{cases} \frac{\pi}{N} (-1)^{i+j} \cot \frac{\pi}{N}(s_i - s_j) & \text{if } i \neq j \\ 0 & \text{if } i = j. \end{cases} \quad (20)$$

Then, (7) becomes

$$\sum_{j=1}^N \Gamma_{jk} w_j = 0 \quad \text{for } k = 1, \dots, N, \quad (21)$$

where the influence coefficients Γ_{jk} are now

$$\Gamma_{jk} = \begin{cases} \frac{1}{\xi_j - \xi_k} \left(\frac{d\xi}{ds} \right)_j + \frac{dC_j}{ds}(s_k) & \text{if } j \neq k \\ - \sum_{i=1, i \neq k}^N \frac{1}{\xi_i - \xi_k} \left(\frac{d\xi}{ds} \right)_i & \text{if } j = k. \end{cases} \quad (22)$$

Unlike the method of Baker et al. (1982) which evaluates the integrand at every other point, the desingularized kernel is evaluated at every nodal point; hence, the matrix is full.

4 Typical Computational Results

4.1 Convergence and stability

The convergence of the spectral method is compared to the piecewise-linear method in Huh and Schultz (1989) for steady test problems. Here, we briefly extend this comparison to time-marching by examining a gravity-wave problem with the initial conditions given by (4) and $a = 0.2$. Fig. 2 compares errors using $N = 16$ for the conservation of energy—the conservation of mass results are very similar. The conservation of energy is determined by $(E(t) - E(0))/E(0)$, where E is given by

$$E = \frac{1}{2} \int \eta^2 dx + \frac{1}{2} \int \phi d\psi. \quad (23)$$

Not only are the results for the spectral computations much more accurate, but they are less computationally intensive. All these computations for $a = 0.2$ can be computed indefinitely without further loss in accuracy (as tested to $t = 200$). The low resolution time computations were made with $\epsilon_t = \epsilon_c = 10^{-4}$ (error criteria for the time-marching and iterative algebraic solver, respectively), the high resolution computations with $\epsilon_t = \epsilon_c = 10^{-10}$. Further refining the time-marching parameters for either method does not improve the computational error. For this initial condition, the spectral computations can give essentially double precision (16 digit) machine accuracy when $N = 32$ and $\epsilon_t = \epsilon_c = 10^{-13}$.

4.2 Steadily progressing wave

We first show that under special circumstances waves of large amplitude do not break. Specifically, we examine gravity waves of permanent form and suppress the Benjamin-Feir instability by applying periodic boundary conditions that do not allow subharmonic disturbances (Longuet-Higgins, 1978). The initial conditions for a steadily progressing wave can be computed from a series expansion as performed by Stokes (1880) and extended using computer algebra by Schwartz (1974). Rather than use series acceleration techniques, we compute the initial conditions for our time-marching code from the iterative method of Schwartz and Vanden-Broeck (1979). We set their surface tension parameter to zero and modify their mapping slightly to desingularize the mapping at very high amplitudes.

Because obtaining accurate initial conditions is the "weak link" in these computations, we compute twice as many points as we use in the time-marching algorithm and discard every other value. To obtain an accurate Jacobian matrix for proper convergence, these computations must be performed in double precision (16 digits). Surprisingly, unless the amplitude is very near the limiting Stokes wave height that forms the 120° crest, single precision is sufficient for the time-marching program.

Figs. 3a-b show eight wave height profiles spaced $\Delta t = 0.5$ apart for the amplitude parameter $(\eta_{max} - \eta_{min})/2\pi = 0.1$ and 0.115 , respectively. The time-marching computations were performed using $N = 64$. The spectral algorithm was used in Fig. 3a, while the more robust piecewise-linear code was required for Fig. 3b since the amplitude is near the Stokes limit of $(\eta_{max} - \eta_{min})/2\pi \approx 0.14$. The computed phase velocities (which are approximately 10.3 and 14.0 percent higher than linear

waves for the cases in Figs. 3a and 3b, respectively), as determined by marching for long time, are accurate to within .005 percent. The RMS variation in the trough to crest wave height is 8×10^{-5} for Fig. 3a and 3×10^{-4} for Fig. 3b. The overdetermined system in this case is twice as accurate as the strong system and only requires 20 percent more CPU time. The spectral computation was again the most accurate, conserving energy and mass to within one part in 10^9 (compared to one part in 10^4 for the equivalent piecewise-linear computations and one part in 10^3 for the higher wave of Fig. 3b). The potential energy was constant to seven significant digits ($PE = 0.1440120$, $KE = 0.15158$) for Fig. 3a and three significant digits for Fig. 3b ($PE = 0.1815$, $KE = 0.19435$).

These waves are not found experimentally, because even if they could be formed, they are subject to a Benjamin-Feir instability (which we suppress with our periodic boundary conditions).

4.3 Simple harmonic linear wave initial conditions

Fig. 4 shows typical results of free surface profiles for dimensionless times 0.1 apart for two different initial amplitudes. The first family of curves for $a = 0.3$ (4) results in a "spilling" breaker. When more energetic initial conditions are used, as in Fig. 4b ($a = 0.544$), the wave becomes a "plunging" breaker. The algorithm breaks down at the last time step shown because of insufficient spatial and/or temporal resolution. This breakdown exhibits itself as a failure of the iterative solution of the algebraic system to converge. The wave profiles change from solid to dashed lines when the spectral solution no longer converges. Until this time, the spectral

(solid line) and piecewise-linear (dashed line) computations are nearly identical although the spectral result is far more accurate. (Slight differences in the profile are shown for the last plotted spectral computation.) This is an indication that the spectral computations are not as robust as the piecewise-linear computations. Our experiences have shown, however, that more precise piecewise-linear computations (by increasing the number of nodes or decreasing the time step) break down sooner. The opposite is true for the spectral computations. We are continuing to study this in an attempt to see if singularities develop in the inviscid model before "breaking" occurs, as in the study of singularity formation in vortex sheets (Krasny, 1986).

We have run numerical simulations for many values of a to determine the initial conditions (4) that cause breaking or spilling. We find that for $a > 0.28$ waves will spill and for $a < 0.27$ waves will progress indefinitely. Typical computations use $N = 60$ or 80 and $\Delta t = 0.1$ or 0.05 . These results are somewhat sensitive to the initial conditions in that an initial condition using a three-term Stokes profile,

$$\eta = a \sin x + 0.5a^2 \sin 2x + 0.375a^3 \sin 3x, \quad (24)$$

does not apply as large a perturbation to the steady form and, hence, the breaking is suppressed to slightly higher amplitudes. This can be seen by examining the limiting case of an "exact" waveform in Fig. 3b, where a $y_{\max} - y_{\min} = .722$ is maintained without breaking. However, a very small subharmonic disturbance would cause these high waves to break.

Since the total energy is constant throughout an entire numerical simulation as well as a (presumably inviscid) experiment, it would appear to be an ideal criterion to determine breaking. Unfortunately, without a very carefully calibrated and

instrumented wavemaker or the ability to measure the velocity everywhere in the flow field, the total energy cannot be measured. Instead, a measured steepness criterion $(\eta_{max} - \eta_{min})/\text{wavelength}$ is usually used. We see from Fig. 5a that this criterion varies widely in time for the two cases with initial conditions (4) of $a = 0.27$ and 0.28 . The peak-to-peak height for the nonbreaking (nonspilling) wave goes higher than the value at a previous time for a wave that breaks. Since (especially the piecewise-linear) computations waves show the wave breaking at less than the maximum peak-to-peak height, the height for a nonbreaking wave could exceed that of a wave that is breaking. There is experimental evidence for this as well (Melville and Rapp, 1988).

However, the potential energy, although not constant in time, is much less variable and can easily be determined from wave probe data. Fig. 5b demonstrates that the computed potential energy for these same two initial conditions are distinct, indicating that potential energy is a better criterion in determining whether a traveling wave will break. These computations show that breaking does not occur at the peak of the potential energy. This could be anticipated since the increased fluid velocities near the crest would increase the kinetic energy at the expense of the potential energy.

It should be noted that the maximum and minimum wave heights are determined at the same instant of time at two different locations for the numerical results of Fig. 5a, while experimental measurements (with one wave probe) are usually measured at one location at two different times.

Figs. 5a and 5b also compare spectral and piecewise-linear computations. The

piecewise-linear computations proceed further before breaking down, but as these computations are refined, they approach the spectral computations and do not proceed as far.

4.4 Convergent wave channel

The growth rate, γ , of equation (7) will cause a wave of any nonzero initial amplitude to break eventually. When the growth rate is large, the wave quickly plunges (Fig. 6a); when it is smaller, after a longer time the wave spills like those seen experimentally (Fig. 6b). The time required for the wave to break, of course, also depends on the initial conditions.

Fig. 7 shows the temporal development of $y_{max} - y_{min}$, the potential energy, and the total energy for a growth parameter $\gamma = 0.2$ and two different initial conditions, $a = 0.1$ and $a = 0.2$. The average growth in the total energy for all cases is exponential at the rate expected, but with small oscillations. These oscillations are not computational errors, but artifacts of the growth model. The potential energy (and hence the kinetic energy) also grow exponentially but with larger oscillations. The lines cease at the point where the computation fails, which for these cases result in wave profiles that appear to be spilling breakers. All computations are spectral except for the dotted line, which shows small deviations of the peak-to-peak measurement near breaking for $a = 0.2$ when the piecewise-linear algorithm is used. In contrast to the no-growth breaking (Figs. 5a and b), these numerical simulations show breaking at or near the maximum values of the peak-to-peak or potential energy measures. The wave grows to a higher value

(by either measure) before breaking when the initial amplitude is smaller. This appears to be caused by the ability of the smaller wave to evolve in time with a wave profile that is more similar to a nonlinear steadily progressive wave.

Breaking wave criteria for waves with varying growth rates can be obtained from Fig. 8. This shows that the breaking criteria (by either peak-to-peak or potential energy measures) increase with the energy input rate, except for a “resonance” phenomena around $\gamma = 0.1$, which appears to be an artifact of the periodic constraints. The data also show dependence on the initial conditions—smaller initial amplitudes adjust to the growth “better” and, hence, break at higher amplitudes.

The dependence of the breaking height has been correlated with growth rate by Van Dorn and Pazan (1975), who have also conducted experiments in a convergent channel. They obtain somewhat higher values of breaking wave height than those of Ramberg and Griffin (1987), which is consistent with the higher convergence rate of their channel, $\epsilon = 1/10$.

4.5 Modelling periodic submerged disturbances

Duncan (1981, 1983) towed hydrofoils to create breaking waves. There are two reasons for using hydrofoils: the first is to avoid separation (which we does not concern our potential flow model), and the second is to apply (negative) values of lift. We could model lift by adding a periodic vortex array to the periodic dipole array, but we choose not to include this effect here. Rather, we “tow” simple dipoles at different speeds and depths and determine the strength of the dipole (the approximate radius of the cylinder) that causes breaking.

We tow the dipole at constant speed starting from rest with homogeneous initial conditions. To avoid an impulse at $t = 0$, which would cause high-frequency waves, we increase the dipole strength exponentially with a time constant of unity, i.e.,

$$a_{dp} = \frac{1}{2} v_{dp} [r_{dp}(1 - e^{-t})]^2. \quad (25)$$

From steady linear theory, the number of waves that should appear in a computational period is equal to $1/v_{dp}^2$ (for our scaling). We have chosen v_{dp} values of 1, 0.707, and 0.5 to represent 1, 2, and 4 wave computations.

Figs. 9a-c show a typical computation for a dipole starting at the origin with a speed equal to 0.5 and unit depth; the strength a_{dp} represents a cylinder of approximately circular cross section with a radius = 0.39 (a larger radius would cause wave breaking). Fig. 9a shows the development of the free surface beginning at rest; initially, a single peak occurs slightly ahead of the dipole. A local maximum in wave height is achieved around $t = 6$, and then the wave puts energy back into the dipole. Fig. 9b shows computations at a later time with a transition between three local maxima and four maxima (four is predicted by linear, steady theory). This transition between the number of peaks is partly responsible for the "beating" rhythm, as seen in the wave diagnostics in Fig. 9c.

Table I shows the maximum value of a_{dp} before breaking occurs (up to $t = 200$) for three combinations of dipole depth and speed as computed by the piecewise-linear algorithm. Often, however, the wave breaks at a lower height as in the constant energy computations in Fig. 5b. The maximum a_{dp} values for the spectral algorithm are somewhat lower, although the wave breaks at approximately the same height. The difference between the algorithms are greater for the dipole case

because the computation is more sensitive to the numerical parameters. The time step had to be significantly smaller in the computations with dipole disturbances although a spatial resolution of $N = 64$ still seemed sufficient.

The potential and total energy are computed as before. While the potential energy representation is the same in this case, the kinetic energy should exclude the kinetic energy inside the cylinder formed by the dipole. This could be computed by integrating $\int \phi d\psi$ in the clockwise direction about the exact cylinder surface. Then conservation of energy could be obtained by knowing the work done by the dipole using Lagally's theorem. This was not attempted here; instead, we compute the "total" energy from the free surface contour only. Mass is still conserved to a high degree (the mean height is 10^{-4} to 10^{-10} of the RMS wave height).

Table I. Wave Breaking Caused by a Periodic Dipole Array

	speed	1	.707	.5
depth				
.5	max a_{dp}	.14	.09	.10
	$y_{max} - y_{min}$.86	.35	.21
	Total Energy	.43	.08	.02
	Potential Energy	.21	.035	.009
	Beat Period	125	130	∞
1	max a_{dp}	.19	.14	.41
	$y_{max} - y_{min}$.86	.35	.2
	Total Energy	.43	.07	.015
	Potential Energy	.21	.03	.008
	Beat Period	130	160	12
2	max a_{dp}	.309	.33	.97
	$y_{max} - y_{min}$.8	.35	.21
	Total Energy	.41	.04	.03
	Potential Energy	.20	.022	.015
	Beat Period	123	200	10

Figs. 10a-b show breaking waves for two different dipole depths. The deeper dipoles tend to produce only one primary peak at $v_{dp} = 0.5$, while shallow dipoles give four as predicted from linear theory. Surprisingly, the peak-to-peak breaking wave heights are about the same, independent of the size of the other nonbreaking peaks.

4.6 Wave modulation and reflection

Experimental waves break at significantly less than the predicted Stokes limiting value, and even less than that predicted here, because of three-dimensional effects, viscous effects, wave reflections from beaches, and the Benjamin-Feir instability. We can test the last effect by taking a larger periodic domain and applying a subharmonic disturbance—a modulated initial condition. Dold and Peregrine (1986) computed recurrence caused by modulation, but did not examine breaking waves. Fig. 11 shows a breaking wave that has a 10 percent modulation of the primary wave for a wavelength twice that of the primary wave. This is the easiest long wave disturbance to model using a periodic algorithm and is the wavenumber that Longuet-Higgins (1978) considers to be most unstable. Specifically, the boundary conditions we apply are those of (4) except that a is a “slowly” varying function of x . For Fig. 11, $a = a'(1 + \delta \cos 2x)$, where $a' = .23$ and $\delta = .10$. From this simple example, we see that a 10 percent modulation of the initial conditions causes an approximately 20 percent reduction in the initial size of a wave that breaks ($a = .28$ is reduced to $.23$).

We also expect that reflection from the beach could cause smaller amplitude

waves to break. These reflections are modeled by

$$\eta = a (\sin x - \mu \cos x) \text{ and } \phi = a (1 + \mu) \cos x, \quad (26)$$

where μ is the reflection coefficient. Fig. 12 shows that, contrary to the the effect of modulation, a 10 percent reflection coefficient modifies the initial conditions for breaking by approximately 5 percent ($a = .28$ is reduced to .265). The plots of $y_{max} - y_{min}$ and potential energy are qualitatively similar to those of Figs. 5a and 5b.

5 Convergent Channel Experiments Compared to Computations

The Naval Research Laboratory (NRL) experiments discussed in this section were conducted in a channel 30m long and 1.3m wide at the wavemaker with about 1.0m mean water depth. The test procedures and the set-up of the experiments are described by Ramberg et al. (1985) and Ramberg and Griffin (1987). The channel was fitted with a convergent section with a rate of 1:16. This generated steep and breaking waves under reasonably well-controlled conditions. Previous breaking wave experiments in a wave channel with a convergent section had been conducted and reported by Van Dorn and Pazan (1975).

Wave heights were measured with capacitance wave probes. The length-scale for the experiments was $g(T/2\pi)^2$, such that the nondimensional spatial period of a linear wave was 2π , in accordance with the periodic computations.

The location of wave breaking was established visually during the experiments as the position along the convergent channel where the sharp wave crests were

first perceived to be “tripping” into a spilling or plunging mode (where we first observed an increase in the crest fluid velocity over that of the traveling waveform. These locations were recorded and later compared to the positions where the measured variation of the average wave height \bar{H} exhibited a transition from growth to attenuation along the channel. In all of the cases compared, there was good agreement between the two estimated locations. Typical examples of spilling and plunging breakers are given in the photographs in Ramberg and Griffin (1987).

Two hundred equally spaced temporal measurements of wave height were taken over eight wavemaker periods with two probes placed 3.0m apart. These measurements were repeated sequentially over twenty-four spatial locations.

It is often difficult to determine the breaking location, especially when breaking is intermittent. Fig. 13 shows how the spectra at the break point can help determine occurrences of wave breaking. The nonbreaking wave has one prominent peak at $k = 8$ since data were taken for eight cycles of the wavemaker at each location. When breaking occurs, the higher harmonics are much more pronounced. Also, the wave numbers below $k = 8$ are larger—indicating greater wave modulation during breaking in these examples.

At each location, for each wavemaker period, a maximum and a minimum height were determined using quadratic interpolation. The mean and standard deviation of the nondimensional peak-to-peak height, H , was determined for the eight cycles at each location. The potential energy (or RMS wave height) of the experimental waves was computed by integrating the square of the height using Simpson’s rule for six to eight full wave periods, as determined by consecutive crossings of the average

datum height level. After computing the mean potential energy, the standard deviation of potential energy between full wave periods was computed. The average RMS value for all data (breaking and nonbreaking) is shown in Fig. 14 as a function of the nondimensional growth rate. The growth rate was determined from (9) even though some data was taken just into the nonconvergent portion of the channel as described by Ramberg, et al. (1985). Those waves determined to be at the point of incipient breaking are marked with closed symbols. The general trend of higher waves for higher growth rates is an indication of the growth of the waves down the channel as the width decreases.

Schultz et al. (1986) and Ramberg and Griffin (1987) found that the dimensional peak-to-peak measurement for *breaking* waves was equal to $0.021 gT^2$, corresponding to $H = .83$ in the present scaling as noted in Fig. 15a. This figure shows that H increases with the growth parameter γ , as predicted in Fig. 7. These predictions are higher than the experimental data—presumably due to three-dimensional, viscous, and wave reflection and wave modulation effects in the experiments. The least-squares linear fit of the breaking data in Fig. 15a is given by

$$H = 0.57 + 7.6\gamma . \quad (27)$$

The standard deviation about this curve is ± 10 percent compared to ± 17 percent for the entire data breaking data of Fig. 15a. The corresponding RMS height (proportional to the square root of potential energy) is shown for breaking waves in Fig. 15b. A least-squares straight line fit for this data has the form

$$RMS = 0.22 + 1.3\gamma , \quad (28)$$

with a deviation of ± 7 percent, significantly better than the variation for H . Also, potential energy (or RMS) reduces scatter in the standard deviation of the measurement at one location. At each breaking event location, standard deviations of H and the RMS wave height for the six to eight cycles are calculated. The mean of these standard deviations is 3.2 percent for $H = y_{max} - y_{min}$ and 2.7 percent for the RMS height. The computations (e.g., Figs. 5b, 9c, 12) also show that potential energy (or equivalently RMS wave height) is "better behaved" than the peak-to-peak values.

Some comparisons of the experimental wave breaking location showed good agreement (within 30 percent) of the computed time of breaking multiplied by the group velocity, when a was chosen from linear steady wavemaker theory.

6 Momentum and Energy Considerations After Breaking

A wide range of wave heights at the *onset of breaking* is shown in Ramberg and Griffin (1987) for a number of recent investigations corresponding to deep water waves. The data from *all* of the experiments employ a crest-to-preceding-trough value for H . The wave heights measured by Ochi and Tsai (1983) for the breaking of steep nonlinear waves in a uniform channel cover the range of $gT^2 = 200$ to 800 cm, while the wave heights measured in the NRL experiments cover the range of $gT^2 = 550$ to 1100 cm. The wave heights measured by Duncan (1983) are in the range of $gT^2 = 100$ to 400 cm and those measured by Bonmarin and Ramamonjariisoa (1985) are in the range of $gT^2 = 350$ to 650 cm. The latter experiments

were conducted to measure the breaking of waves in a uniform channel, while in the experiments of Duncan the breaking waves were generated by towing a hydrofoil through still water at various submergence depths. Above a critical submergence depth of the hydrofoil, wave breaking occurred spontaneously (Duncan, 1983).

It is also possible to compare the results of Ramberg and Griffin (1987) with the measurements of momentum flux losses by Melville and Rapp (1985). The latter reported measurements of wave breaking in packets of waves generated in a uniform channel by the superposition of Fourier components over a small band centered on the frequency f_o . The integrated wave amplitude a^2 was assumed by Melville and Rapp to be a measure of the momentum flux, ΔS , due to breaking and was determined locally by taking the difference between the incipient breaking condition and conditions farther downstream (normalized by the upstream reference value S_o). The *rate* of momentum flux loss R'_b can be expressed as (Melville and Rapp, 1985)

$$R'_b = \frac{\Delta S/S_o}{\Delta k_o(x - x_b)}, \quad (29)$$

where $k_o = \omega_o^2/g$ for deep water waves, when ω_o is the angular frequency. A comparison between the experiments of Ramberg and Griffin and those of Melville and Rapp (1985) can be made directly from the results in Table II. Only the initial *rates* of energy loss are compared here because during the convergent channel experiments the energy and momentum losses rarely reached an asymptotic value, i.e., the waves continued to break throughout the measurement interval. It should be noted that the rate of momentum flux loss from the experiments of Ramberg and Griffin is derived from estimates of potential energy based upon measured

wave heights. However, there is only a difference of 2π between the loss rates of potential energy and momentum flux.

The results of the two experiments are in agreement that the initial rates of momentum flux loss due to plunging breakers are typically about twice those of spilling breakers. Moreover, the results of Melville and Rapp also indicate that the *total* losses for the two types of breakers differ by about the same factor. The smaller momentum flux losses reported by Melville and Rapp are expected since their results are for the integral momentum flux of a group of waves. It is possible to qualitatively reconcile the loss rates magnitudes given in Table II if about half of the most energetic waves in each packet are actually breaking at any given time.

Table II. Momentum Flux Losses in Wave Breaking

Breaker Type	Wave Steepness	ak	Momentum Flux Loss, R'_b	
Spilling	0.30 ⁺	0.31–0.38 ⁺⁺	0.023 ⁺	0.048 ⁺⁺
Plunging	0.39	0.33–0.38	0.045 ⁺	0.089 ⁺⁺

⁺Melville and Rapp (1985), ⁺⁺Ramberg and Griffin (1987).

7 Concluding Remarks

Computations indicate that the potential energy of surface gravity waves are a better criterion for the onset of breaking for steep nonlinear waves than the wave height. The computed wave height or steepness appear to have more erratic variations in time than the potential energy. The potential energy also reduces the apparent scatter observed in laboratory measurements of individual breaking events.

There are three experimental indications that the square root of the potential energy is better than the peak-to-peak (or steepness) criteria in predicting the onset of breaking events. These are (1) a better correlation to a least-squares fit with x with only two-thirds of the scatter that the peak-to-peak correlation gives, (2) a smaller percentage standard deviation around the mean value at an individual location (breaking or nonbreaking), and (3) a smaller mean percentage variation of individual breaking events from a breaking criteria.

Either breaking criteria (peak-to-peak or potential energy) have been shown to depend on the energy input rate, with the smallest values occurring when the energy input rate is small and spilling breakers are expected. This dependence further explains the scatter of breaking criteria in the convergent channel experiments.

Continuing studies show that the peak-to-peak wave heights and potential energy that can be sustained without breaking are relatively independent of the method of wave formation. We find that the computations tend to show a higher breaking criteria than the experiments, although this difference can be lessened somewhat by modelling wave modulation and to a lesser degree, wave reflection.

The work at The University of Michigan was supported by Naval Research Laboratory Contract No. N00014-85-K-Z019, ONR Ocean Engineering Division Contract N00014-87-0509, and the Program in Ship Hydrodynamics at The University of Michigan, funded by the University Research Initiative of the Office of Naval Research, Contract No. N000184-86-K-0684. The authors acknowledge D.T. Rowley's contribution to the data reduction and L. Pall's editorial assistance.

8 References

- Baker, G.R., D.I. Meiron and S.A. Orszag (1982), Generalized vortex methods for free-surface flow problems, *J. Fluid Mech.* **123**, 477-501.
- Bonmarin, P. and A. Ramamonjiarisoa (1985), Deformation to breaking of deep water gravity waves, *Exp. in Fluids* **3**, 11-16.
- Boyd, J. (1989), *Fourier and Chebyshev Spectral Methods*, Springer-Verlag.
- Cokelet, E.D. (1977), Breaking waves, *Nature* **267**, 769-774.
- Cokelet, E.D. (1977), Steep gravity waves in water of arbitrary uniform depth, *Proc. R. Soc. Lond. A* **286**, 183-230.
- Dold, J.W. and D.H. Peregrine (1984), Steep unsteady water wave: An efficient computational scheme, School of Mathematics University of Bristol Internal Report AM-84-04.
- Dold, J.W. and D.H. Peregrine (1986), Water-wave modulation, School of Mathematics, Univ. of Bristol Report AM-86-03, presented at 20th Int. Conf. on Coastal Eng., Taipei.
- Dommermuth, D.G., D.K. Yue, W.M. Lin, R.J. Rapp, E.S. Chan, and W.K. Melville (1988), Deep-water plunging breakers: a comparison between potential theory and experiments. *J. Fluid Mech.* **189**, 423-442.

- Duncan, J.H., L.A. Wallendorf, B. Johnson (1987), An experimental investigation of the kinematics of breaking waves, Rept. EW-7-87, U.S. Naval Academy.
- Duncan, J.H. (1981), An experimental investigation of breaking waves produced by a towed hydrofoil, *Proc. R. Soc. Lond.* **A377**, 331-348.
- Duncan, J.H. (1983), The breaking and non-breaking wave resistance of a two-dimensional hydrofoil, *J. Fluid Mech.* **126**, 507-520.
- Griffin, O.M. (1984), The breaking of ocean surface waves, *Naval Research Lab. Memorandum Rept. 5997*, Washington D.C.
- Griffin, O.M., R.A. Skop, G.A. Keramidas, T.F. Swean, Jr., H.T. Wang, and Y. Leipold (1989), Ocean and ship wave modification by a surface wake flow patterns, *Proc. 17th Symposium in Naval Hydrodynamics*, National Academy Press, Washington D.C., in press.
- Huang, N.E., L.F. Bliven, S.R. Long, and C.C. Tung (1986), An analytical model for oceanic whitecap coverage, *J. Phys. Oceanog.* **16**, 1597-1604.
- Huh, J. and W.W. Schultz (1989), Spectral boundary integral methods for gravity-capillary waves, in preparation.
- Kjeldsen, S.P. and D. Myrhaug (1978), Kinematics and Dynamics of breaking waves—Main report, VHL Report, Norway.
- Krasny, R. (1986), A study of singularity formation in a vortex sheet by the point-vortex approximation, *J. Fluid Mech.* **167**, 65-93.

- Lin, W.-H., J. N. Newman and D. K. Yue (1984), Nonlinear forced motions of floating bodies, *15th Symposium in Naval Hydrodynamics*, Hamburg.
- Longuet-Higgins, M.S. (1981), A parametric flow for breaking waves, *Hydrodynamics in Ocean Engineering*, Norwegian Inst. Tech., 121-135.
- Longuet-Higgins, M.S. (1985), Accelerations in steep gravity waves, *J. Phys. Oceanog.* **15**, 1570-1579.
- Longuet-Higgins, M.S. and E. D. Cokelet (1976), The deformation of steep surface waves on water: I. A numerical method of computation, *Proc. R. Soc. Lond.* **A350**, 1-26.
- Longuet-Higgins, M.S. (1978), The instabilities of gravity waves of finite amplitude in deep water: II. Subharmonics, *Proc. R. Soc. Lond.* **A360**, 489-505.
- McIver, P. and D.H. Peregrine (1981), Comparison of numerical and analytical results for waves that are starting to break, *Hydrodynamics in Ocean Engineering*, Norwegian Inst. of Tech., 203-215.
- Melville, W.K. (1982), The instability and breaking of deep-water waves, *J. Fluid Mech.* **115**, 165-185.
- Melville, W.K. and R.J. Rapp (1985), Momentum flux in breaking waves, *Nature* **317**, 514-516.
- Melville, W.K. and R.J. Rapp (1988), The surface velocity field in steep and breaking waves, *J. Fluid Mech.* **189**, 1-22.

- Ochi M.K. and C.-H. Tsai (1983), Prediction and occurrence of breaking waves in deep water, *J. Phys. Oceanography* **13**, 2008-2019.
- Ramberg, S.E. and O.M. Griffin (1984), Laboratory studies of steep and breaking deep water waves, Proceedings of the 5th Engineering Mechanics Division Specialty Conf., ASCE, Laramie, WY:712-715.
- Ramberg, S.E. and O.M. Griffin (1987), Laboratory studies of steep and breaking deep water waves, Proc. ASCE, *J. Waterways, Port, Coastal and Ocean Engineering* **113**:493-506.
- Ramberg, S.E., M.E. Barber, and O.M. Griffin (1985), Laboratory studies of steep and breaking deep water waves in a convergent channel, *Naval Research Laboratory Memorandum Rep. 5610*, Washington, D.C.
- Roberts, A.J. (1983), A stable and accurate numerical method to calculate the motion of a sharp interface between fluids, *IMA J. Appl. Math.* **31**, (1983).
- Schultz, W.W. (1985), Integral equation algorithm for breaking waves, 10th IMACS World Congress, Oslo, Norway.
- Saad, Y. and M.H. Schultz (1986), GMRES: A generalized minimal residual algorithm for solving nonsymmetric linear systems, *SIAM J. Sci. Stat. Comput.* **7**, 856-869.
- Schultz, W.W and S.-W. Hong (1989), A complex boundary integral method for two dimensional potential problems, *J. Comp. Phys.* **84**, 414-440.

- Schwartz, L.W. (1974), Computer extension and analytic continuation of Stokes' expansion for gravity waves, *J. Fluid Mech.* **62**, 553-78.
- Schwartz, L.W. and J.-M. Vanden-Broeck (1979), Numerical solution of the exact equations for capillary-gravity waves, *J. Fluid Mech.* **95**, 119-139.
- Srokosz, M.A. (1986), On the probability of wave breaking in deep water, *J. Phys. Oceanog.* **16**, 382-385.
- Stokes, G.G. (1880), Supplement to a paper on the theory of oscillatory waves, *Math. and Phys. Papers.* **1**, 314-326.
- Vanden-Broeck, J.-M. (1980), Nonlinear stern waves, *J. Fluid Mech.* **96**, 603-611.
- Van Dorn, W.G. and S.P. Pazan (1975), Laboratory investigation of wave breaking. II: Deep water waves, Scripps Inst. Oceanog. Rep. 75-21.
- Vinje, T. and P. Brevig (1981), Numerical simulation of breaking waves, *Adv. Water Resources* **4**, 77-82.

Figure Captions

- 1 Problem Domain
 - a. physical (ξ) space
 - b. mapped (ζ) space

- 2 Comparison of errors for energy conservation ($N = 32$)

	piecewise-linear (total cpu seconds = 186)
	spectral, high time resolution (total cpu seconds = 28)
	spectral, low time resolution (total cpu seconds = 100)

- 3 Steadily progressing wave profiles
 - a. $y_{max} - y_{min} = 0.1$. (spectral)
 - b. $y_{max} - y_{min} = 0.115$. (piecewise-linear)

- 4 Free surface profiles ($\Delta t = .1$, $N = 32$)
 - a. spilling breaker ($a = 0.3$)
 - b. plunging breaker ($a = 0.544$)

- 5a Peak-to-peak wave heights for $a = 0.27, 0.28$

	spectral $N = 32$, — — — piecewise-linear $N = 32$, $N = 64$
--	--
- 5b Potential energy for same two initial conditions

	spectral $N = 32$, — — — piecewise-linear $N = 32$, $N = 64$
--	--

- 6a Wave profiles with rapid exponential growth

$\gamma = .5$, increment between plotted profiles $\Delta t = 0.2$
(except last increment $\Delta t = 0.1$)
- 6b Wave profiles with slow exponential growth

$\gamma = .02$, increment between plotted profiles $\Delta t = 0.2$

- 7 Evolution of wave diagnostics with growth parameter $\gamma = 0.2$
two initial wave heights, $a = .1, .2$, spectral computations

	$y_{max} - y_{min}$
	potential energy
	total energy
	piecewise-linear results for $y_{max} - y_{min}$

- 8 Breaking criteria for exponential growth conditions

	$y_{max} - y_{min}$
	potential energy

- 9a Wave profiles caused by a moving dipole (initial development)
 $v_{dp} = .5, r_{dp} = .39, d_{dp} = 1, 0 \geq t \geq 10$
- 9b Wave profiles caused by a moving dipole (intermediate development)
 $v_{dp} = .5, r_{dp} = .39, d_{dp} = 1, 20 \geq t \geq 23$
- 9c Wave diagnostic for profiles caused by a moving dipole
 _____ $y_{max} - y_{min}$
 - - - - - potential energy
 - . - . - . - total energy
 corresponding curves for a breaking wave $r_{dp} = .42$
- 10a Breaking profile for shallow dipole ($v_{dp} = .5, r_{dp} = .11, d_{dp} = .5$)
- 10b Breaking profile for deep dipole ($v_{dp} = .5, r_{dp} = .99, d_{dp} = 2.0$)
- 11 Breaking modulated periodic wave
 initial modulation is 10 percent with wavelength twice that of the primary wave.
 - - - - - initial wave profile
 _____ profile at breaking, $t = 97.0, 97.2, 97.4, 97.6$
- 12 Breaking wave with reflection
 reflection coefficient is 10 percent with initial amplitude $a = .265$
 _____ $y_{max} - y_{min}$
 - - - - - potential energy
- 13 Fourier coefficients for wave data (experiments from Ramberg et al., 1985)
 - - - - - breaking wave
 _____ nonbreaking wave
- 14 RMS wave height for all data (experiments from Ramberg et al., 1985)
 (solid symbols denote incipient breaking waves)
- 15a Peak-to-peak height for breaking waves (experiments from Ramberg et al., 1985)
- 15b RMS height results for breaking waves (experiments from Ramberg et al., 1985)

Fig. 1a

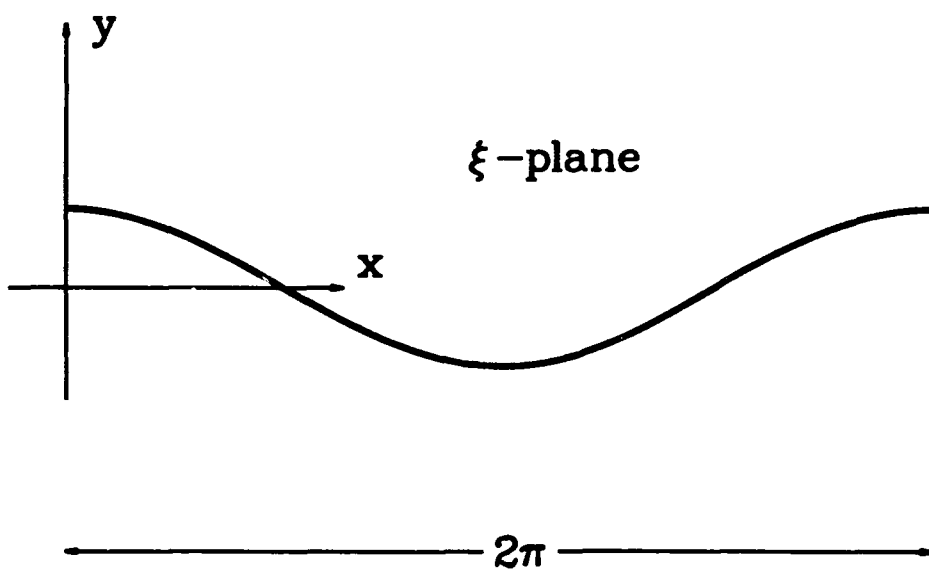


Fig. 1b

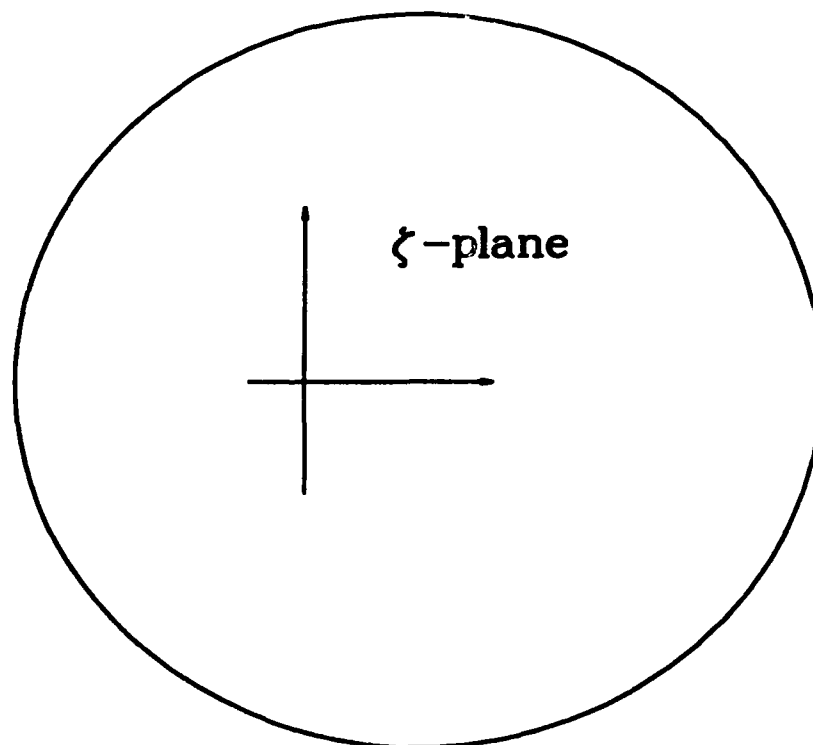


Fig. 2

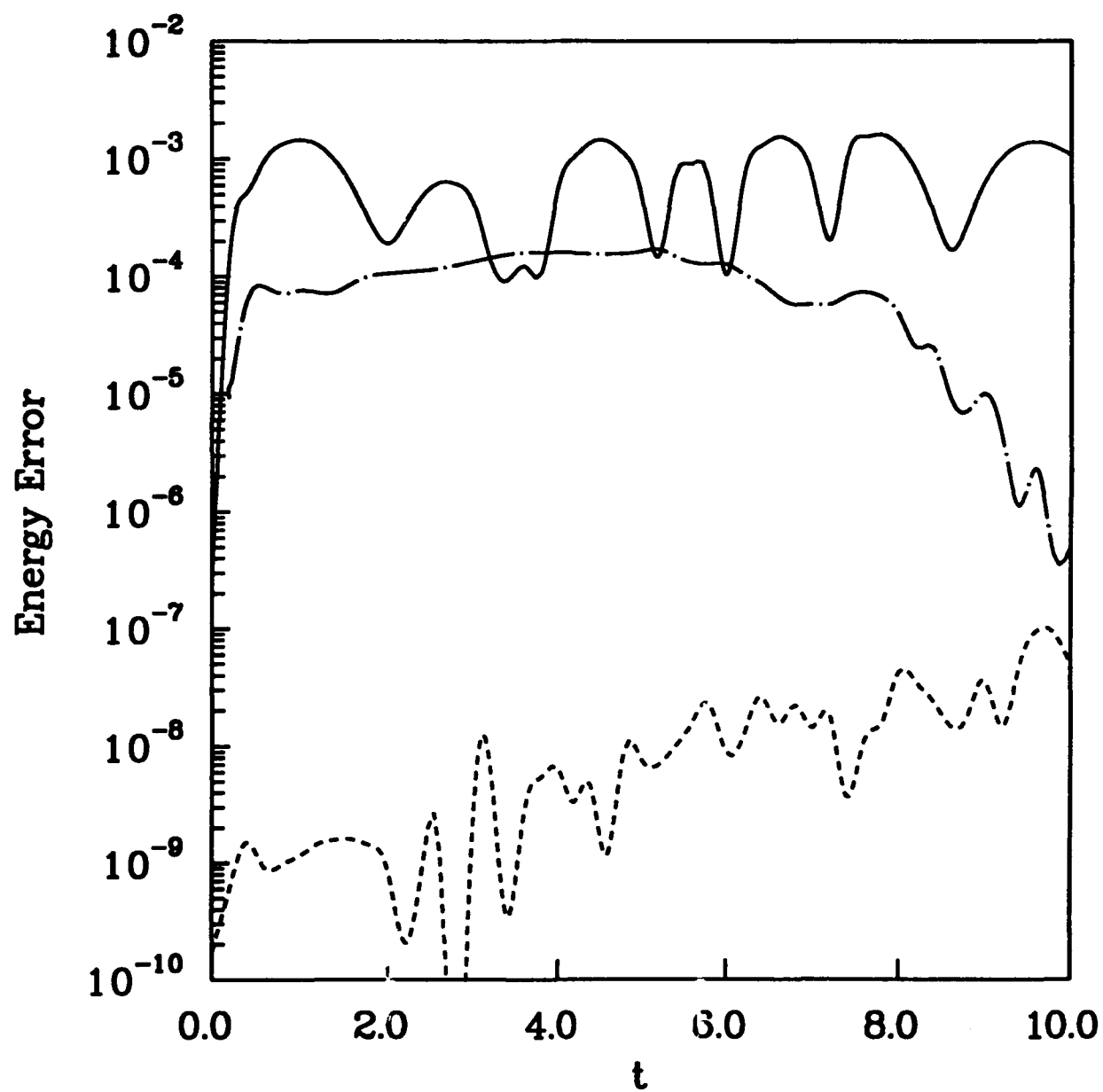


Fig. 3a

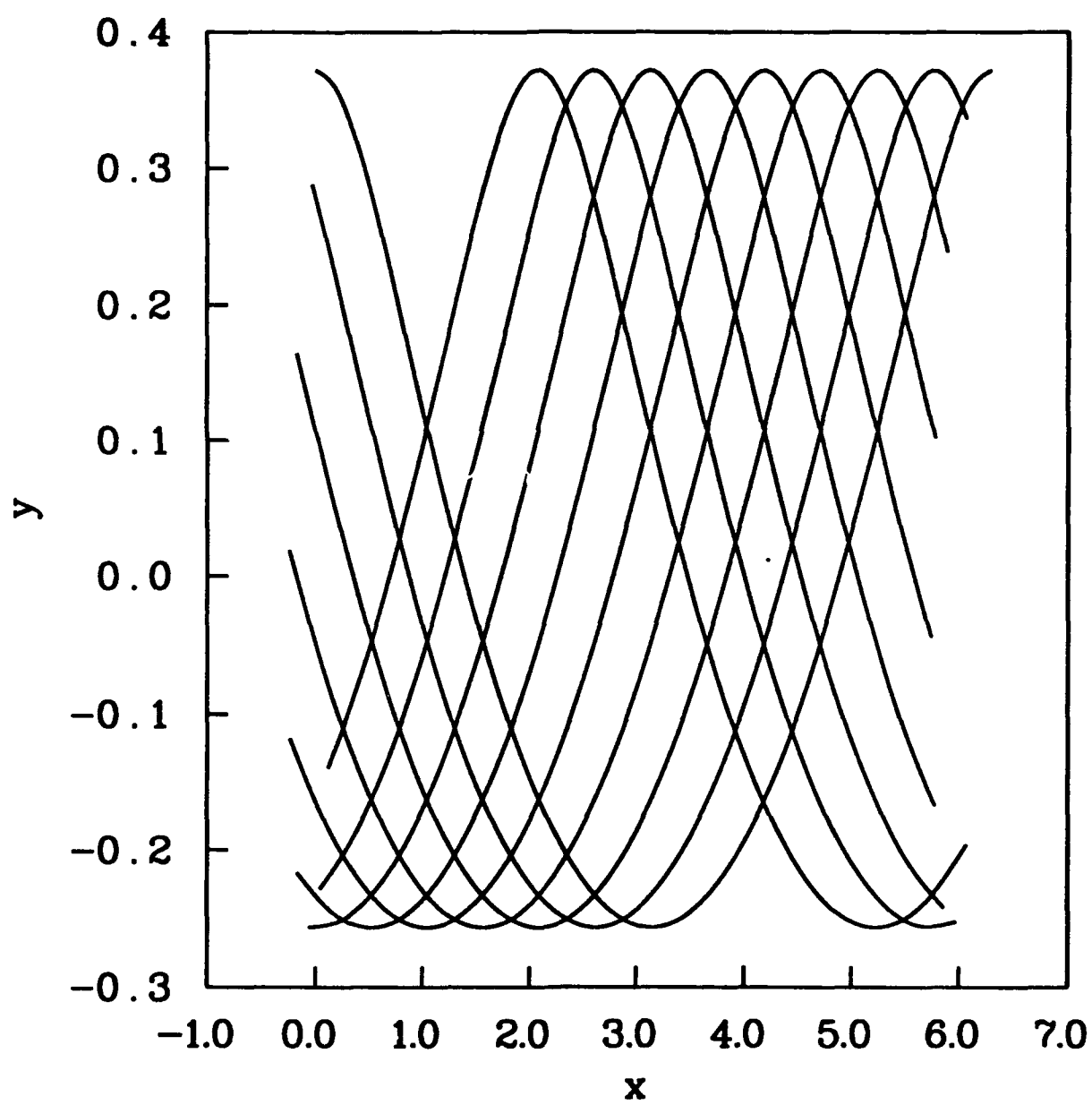


Fig. 3b

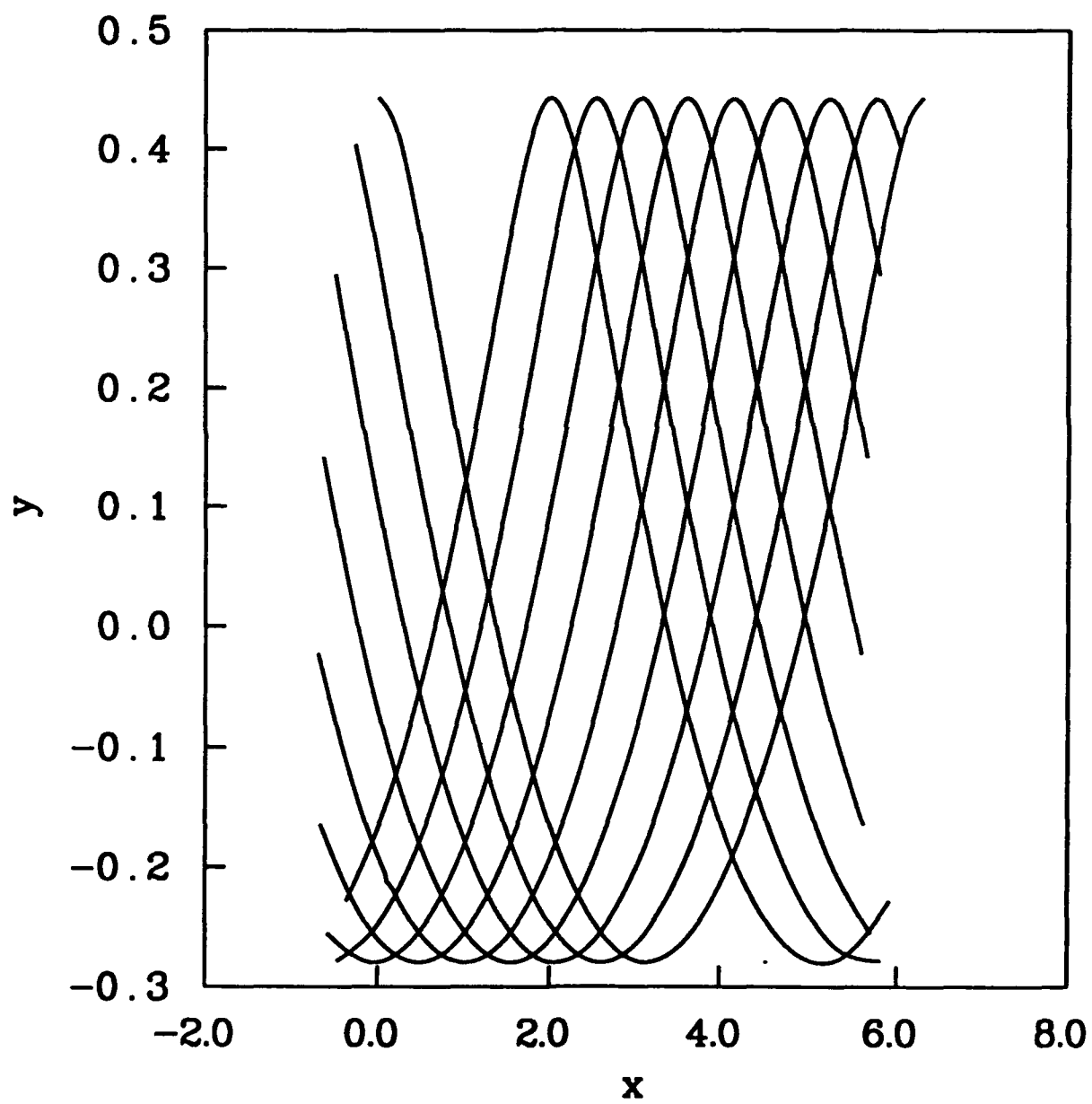


Fig. 4a

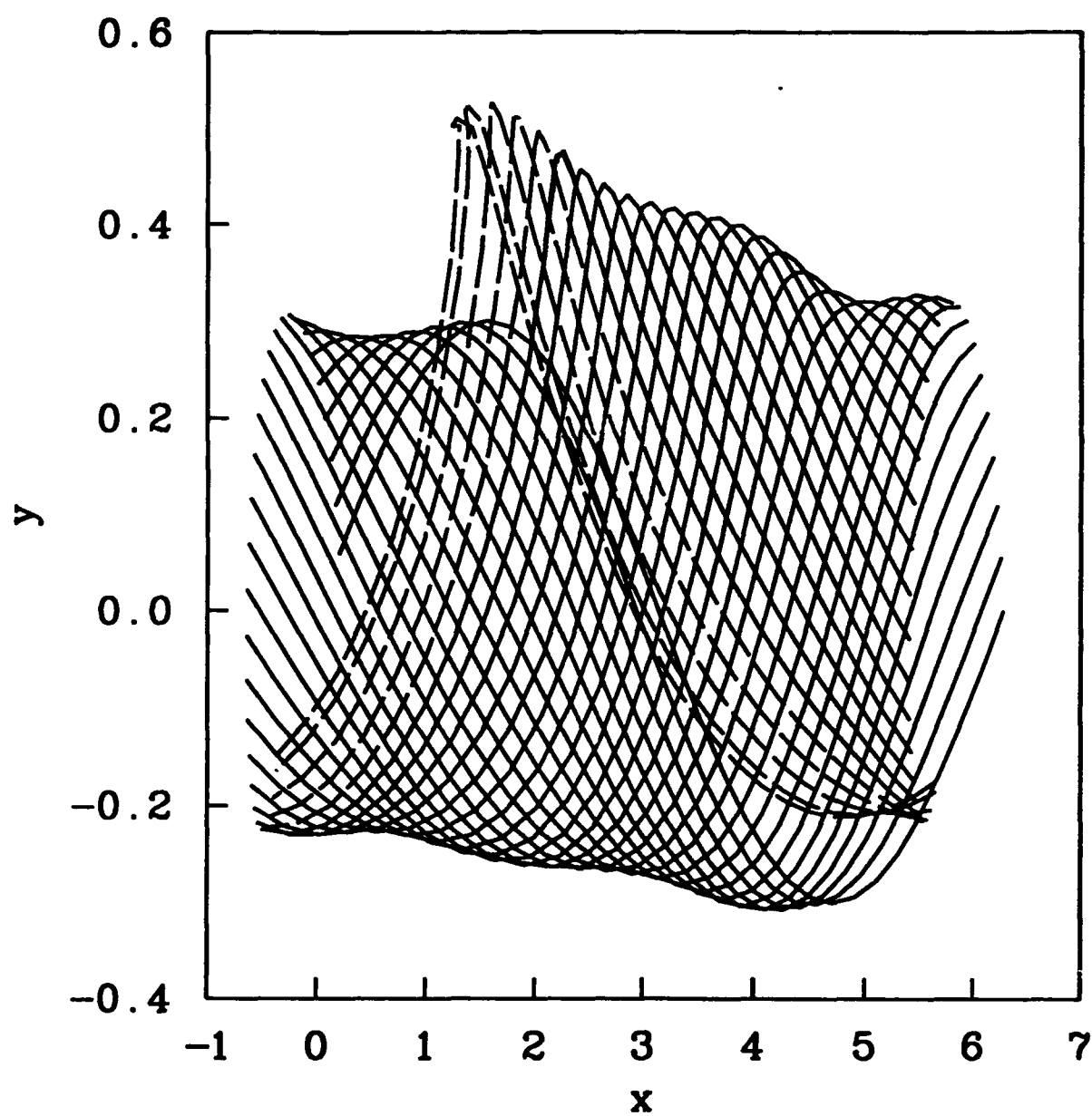


Fig. 4b

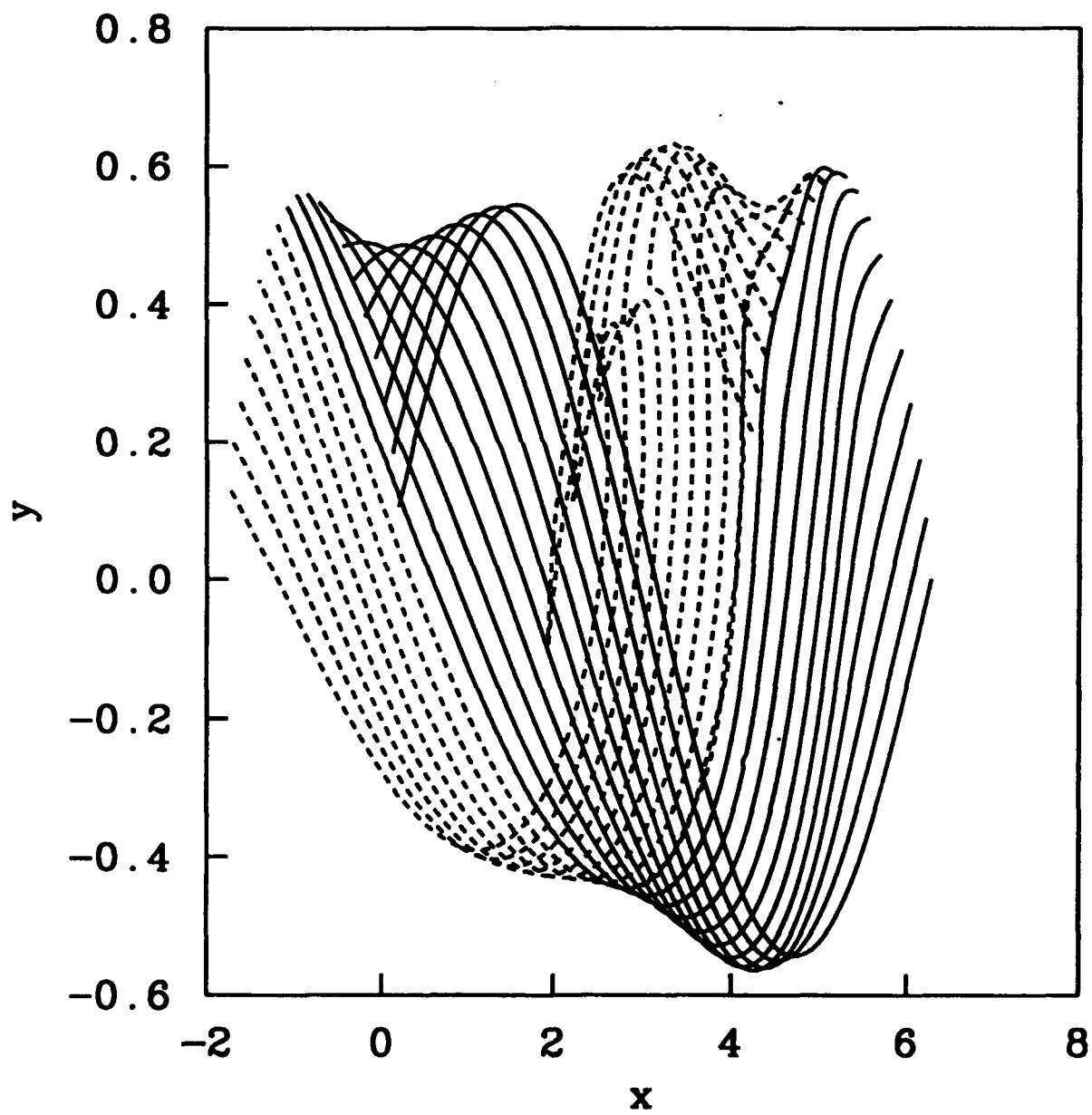


Fig. 5a

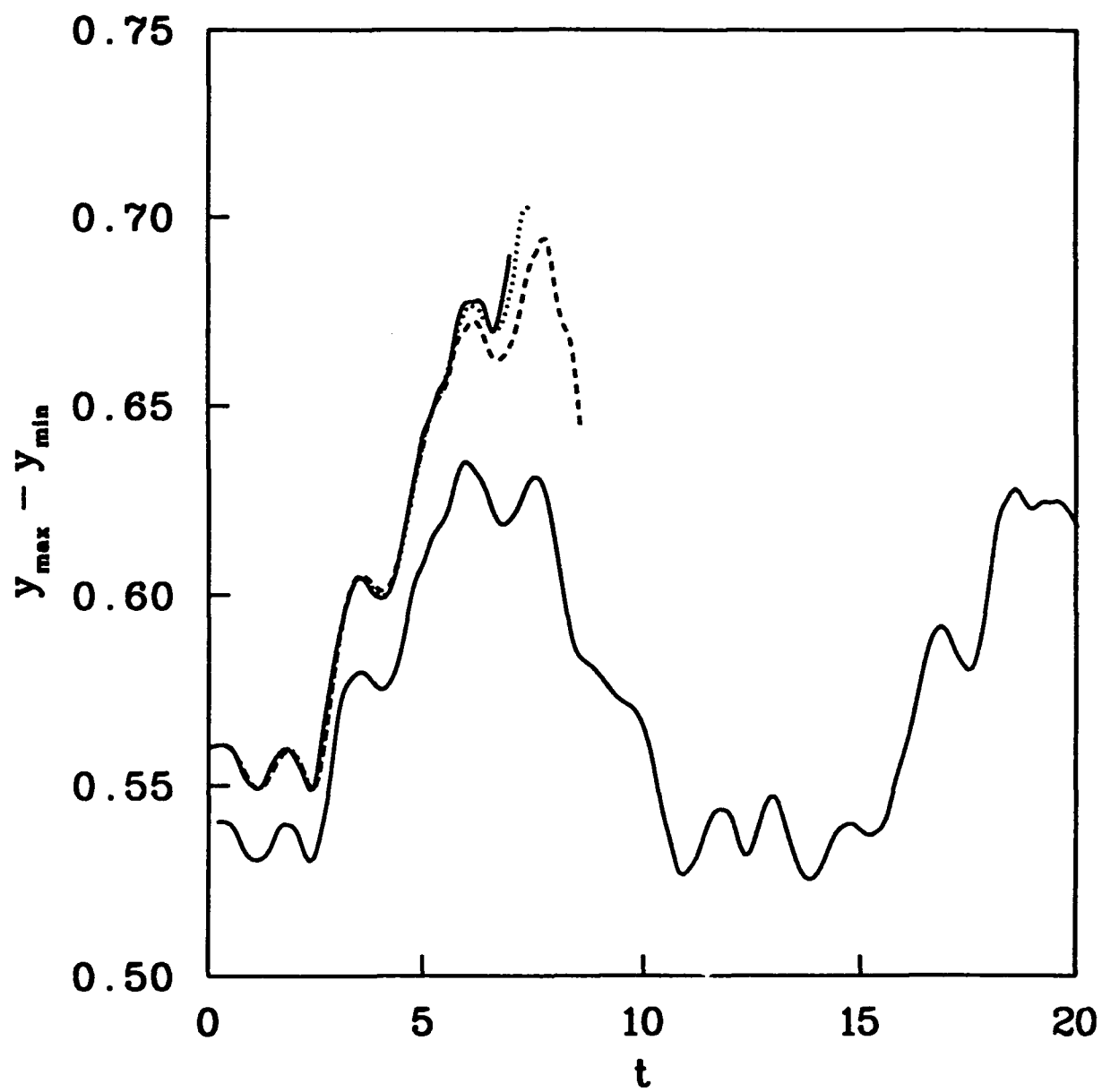


Fig. 5b

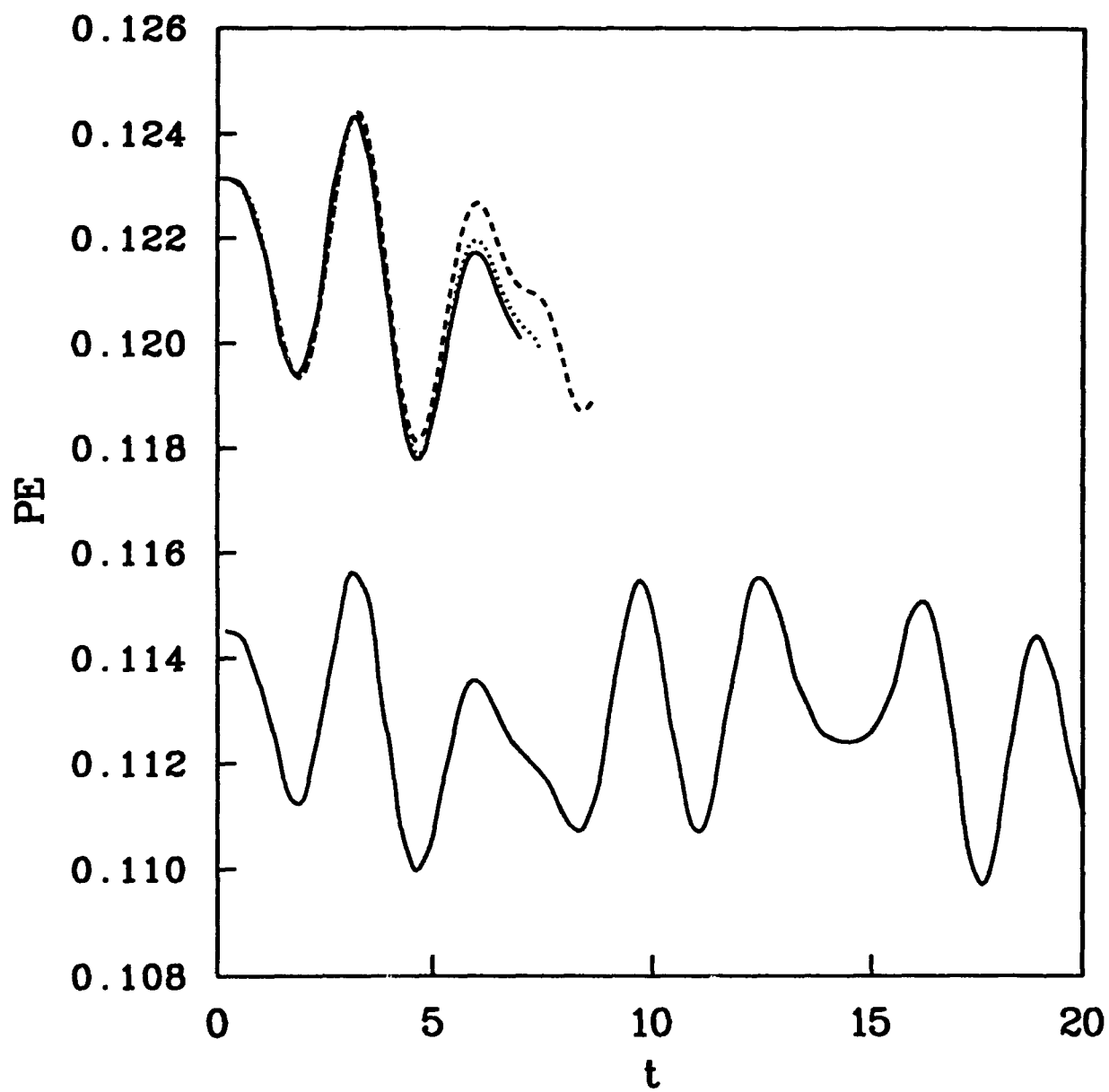


Fig. 6a

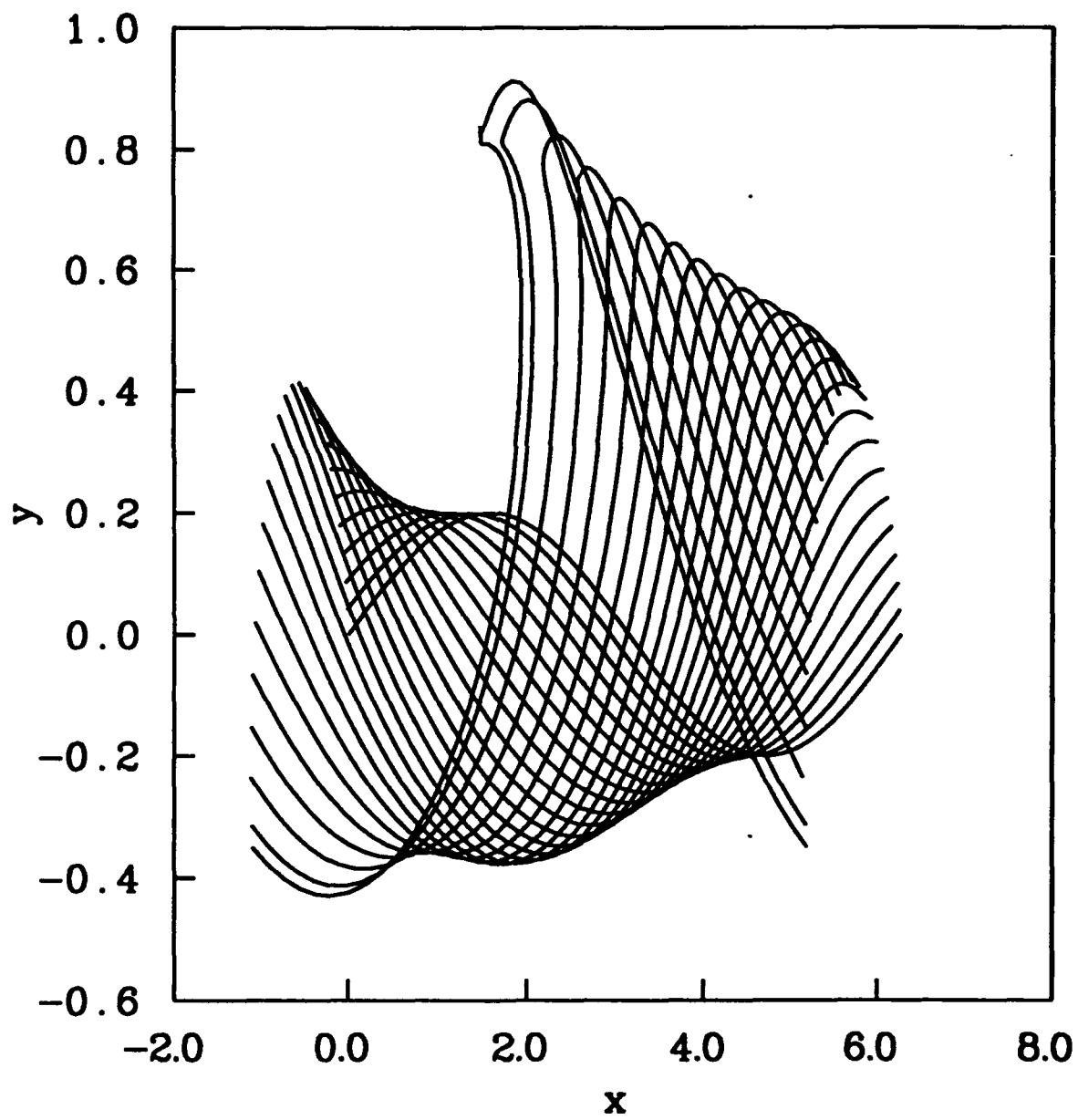


Fig. 6b

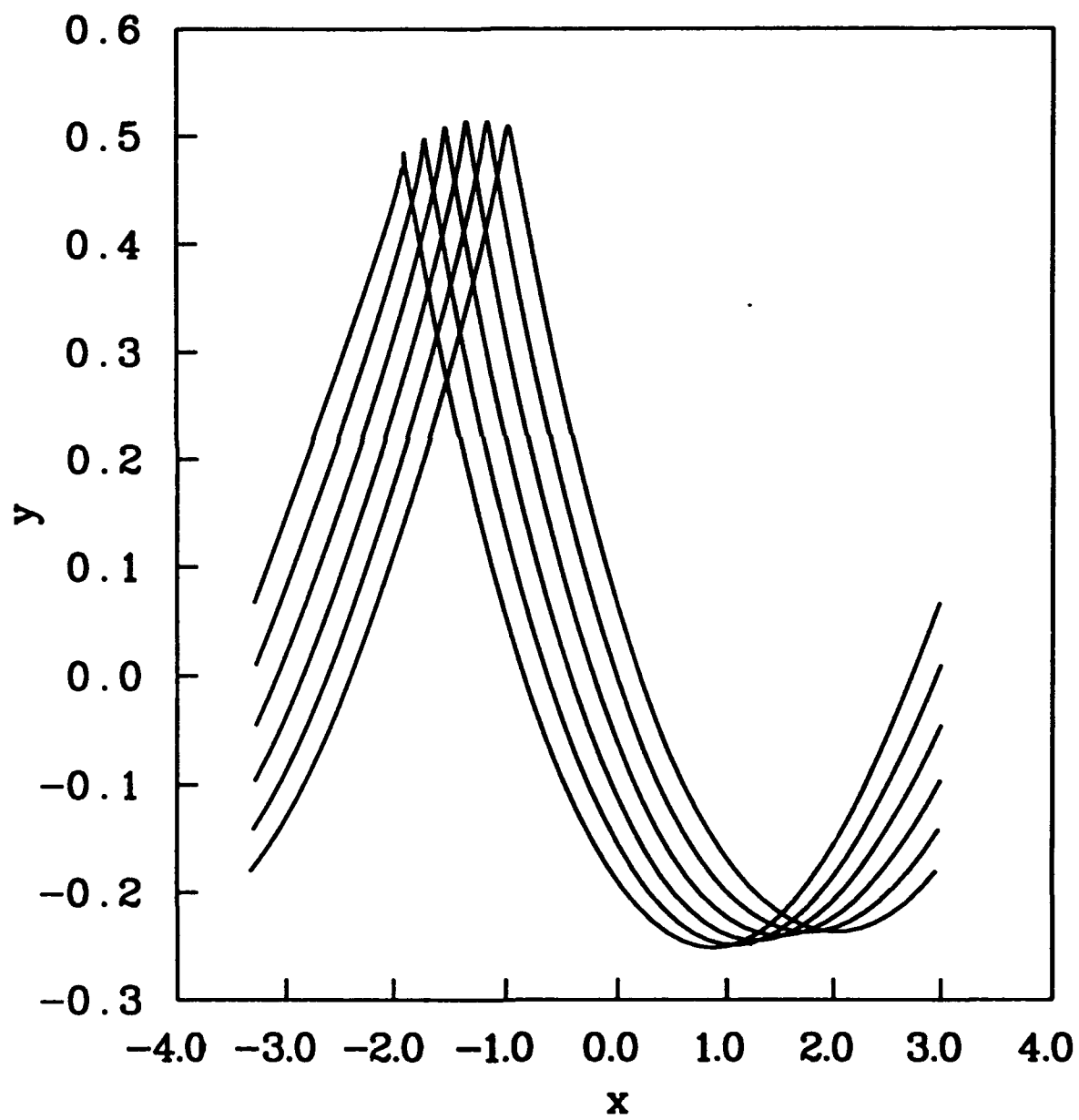


Fig. 7

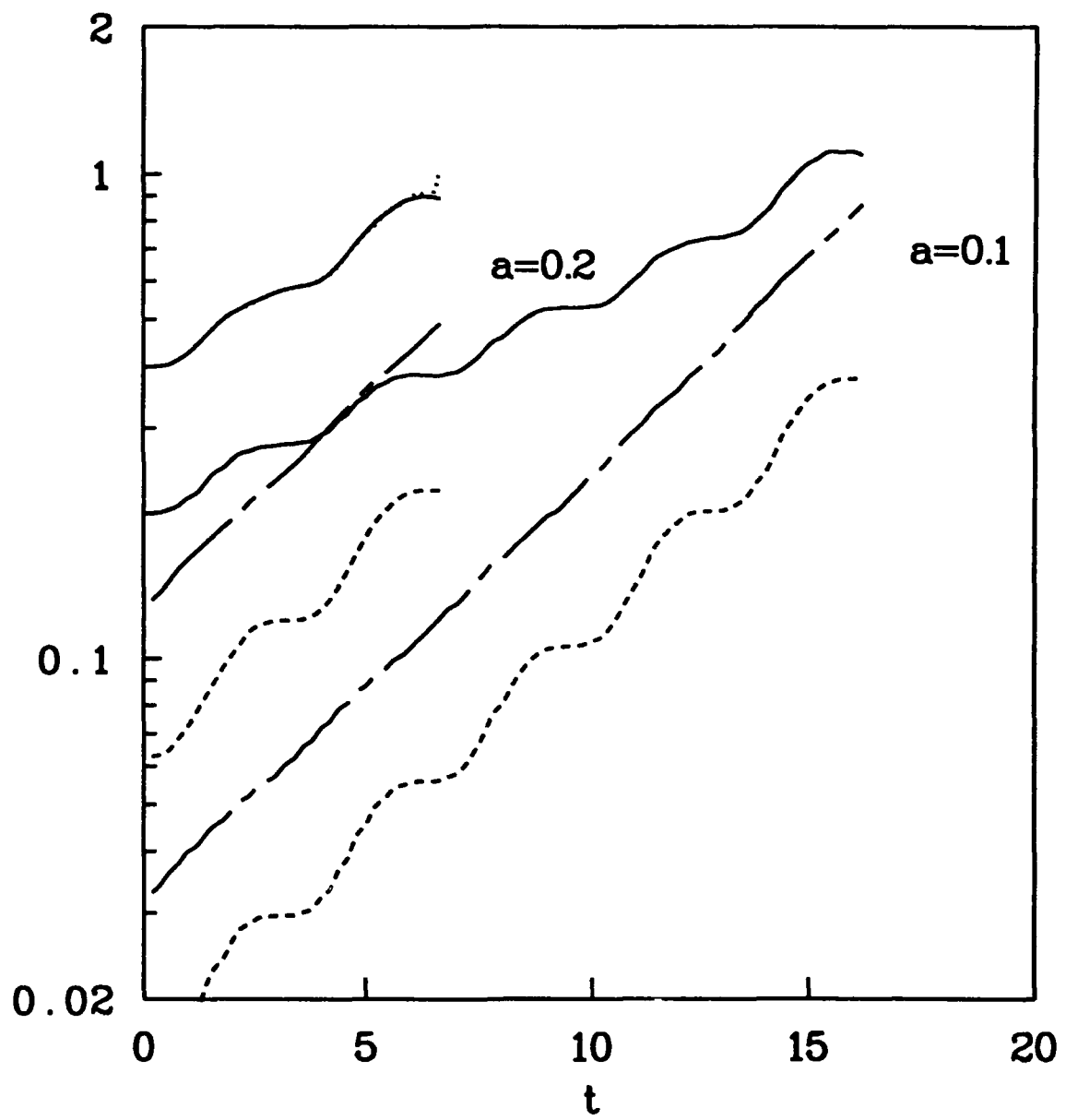


Fig. 8

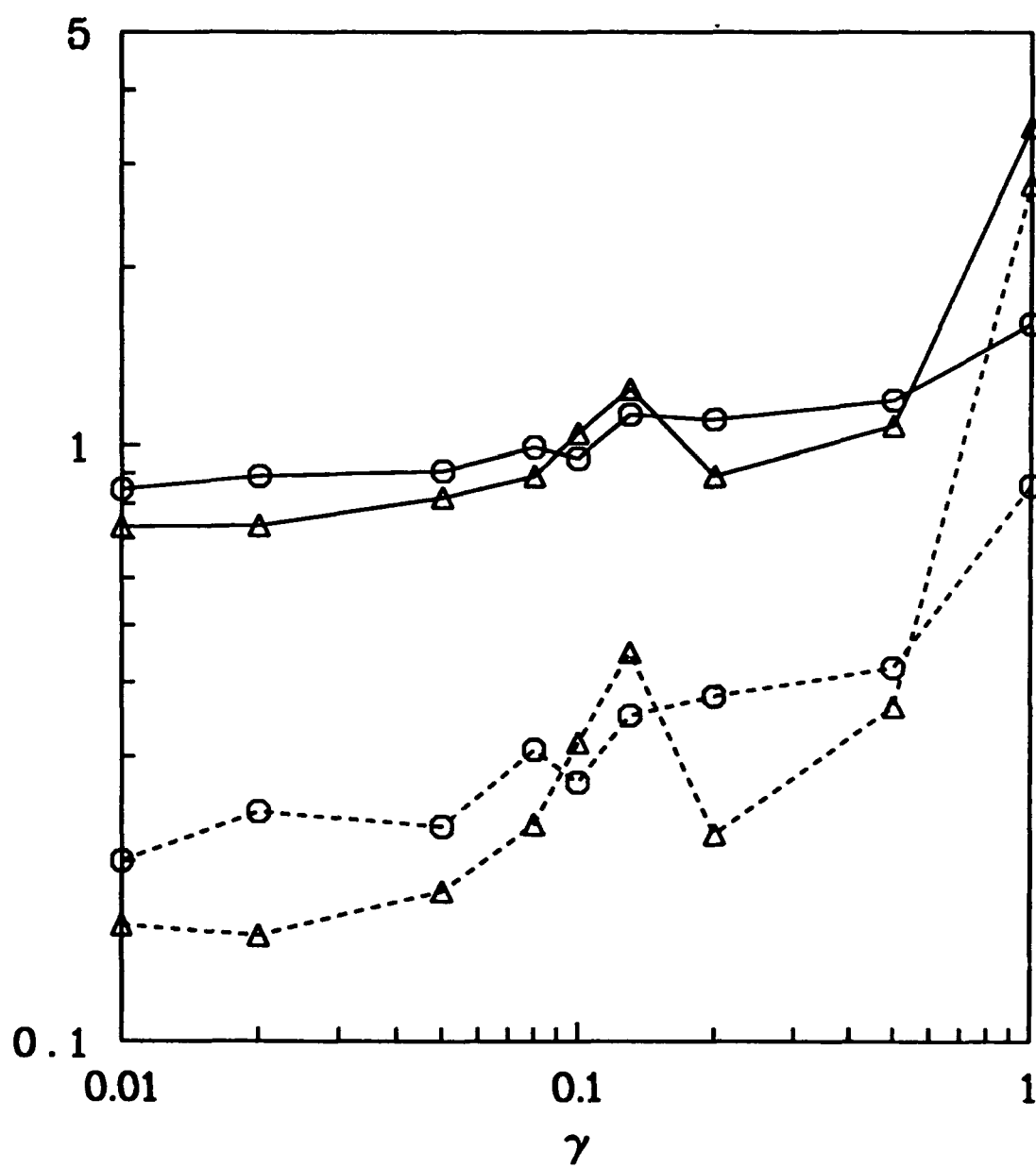


Fig. 9a

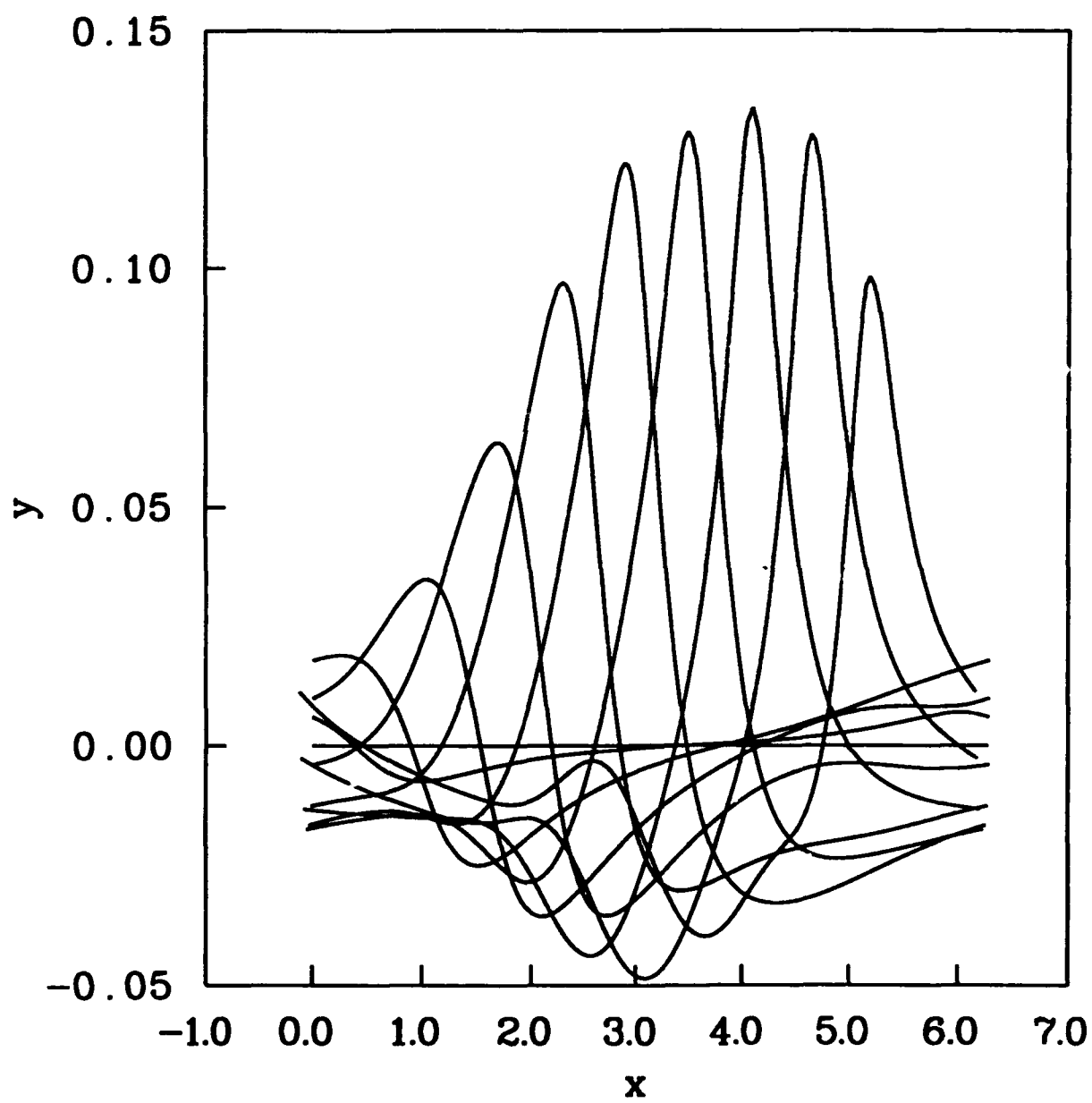


Fig. 9b

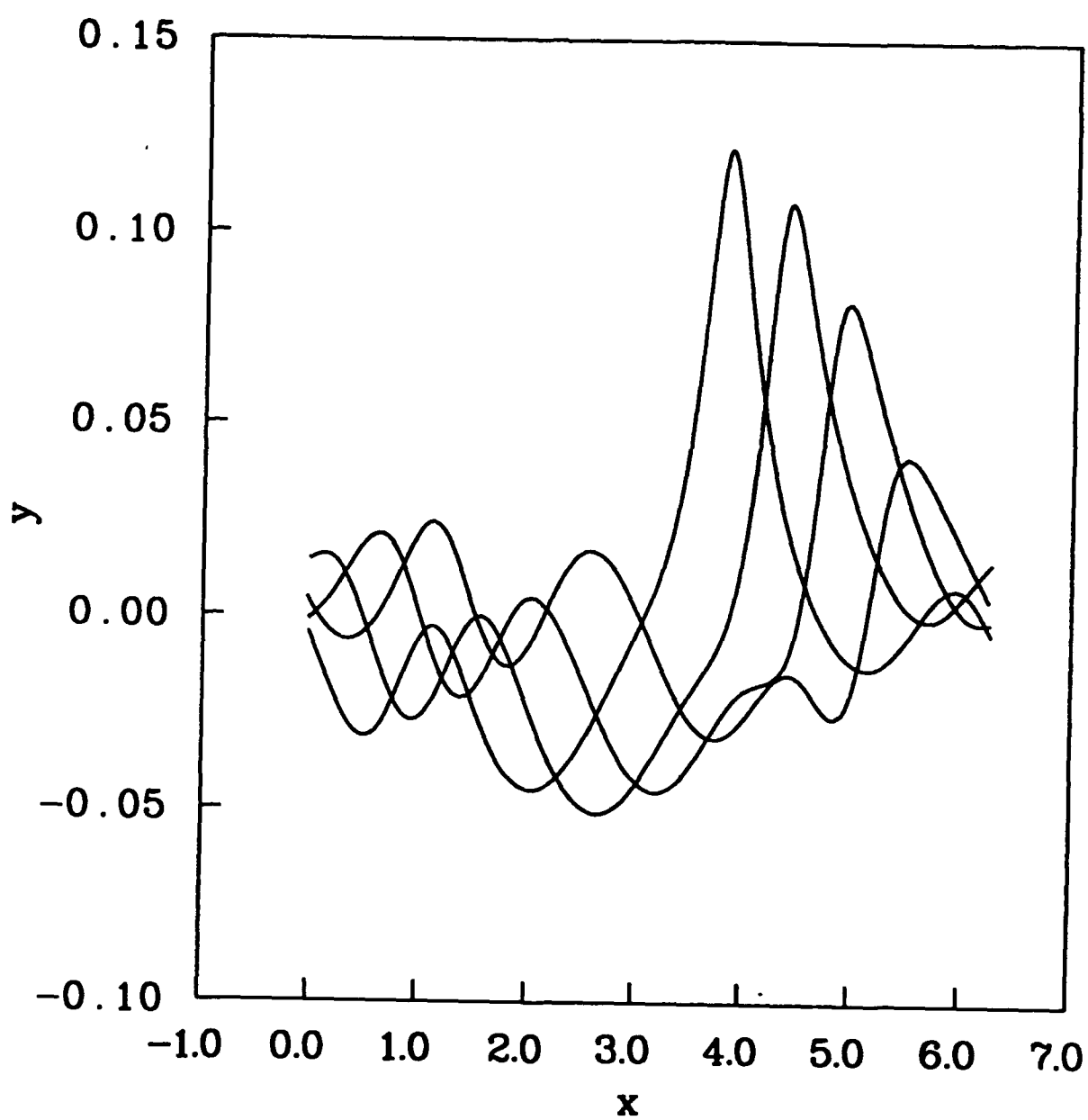


Fig. 9c

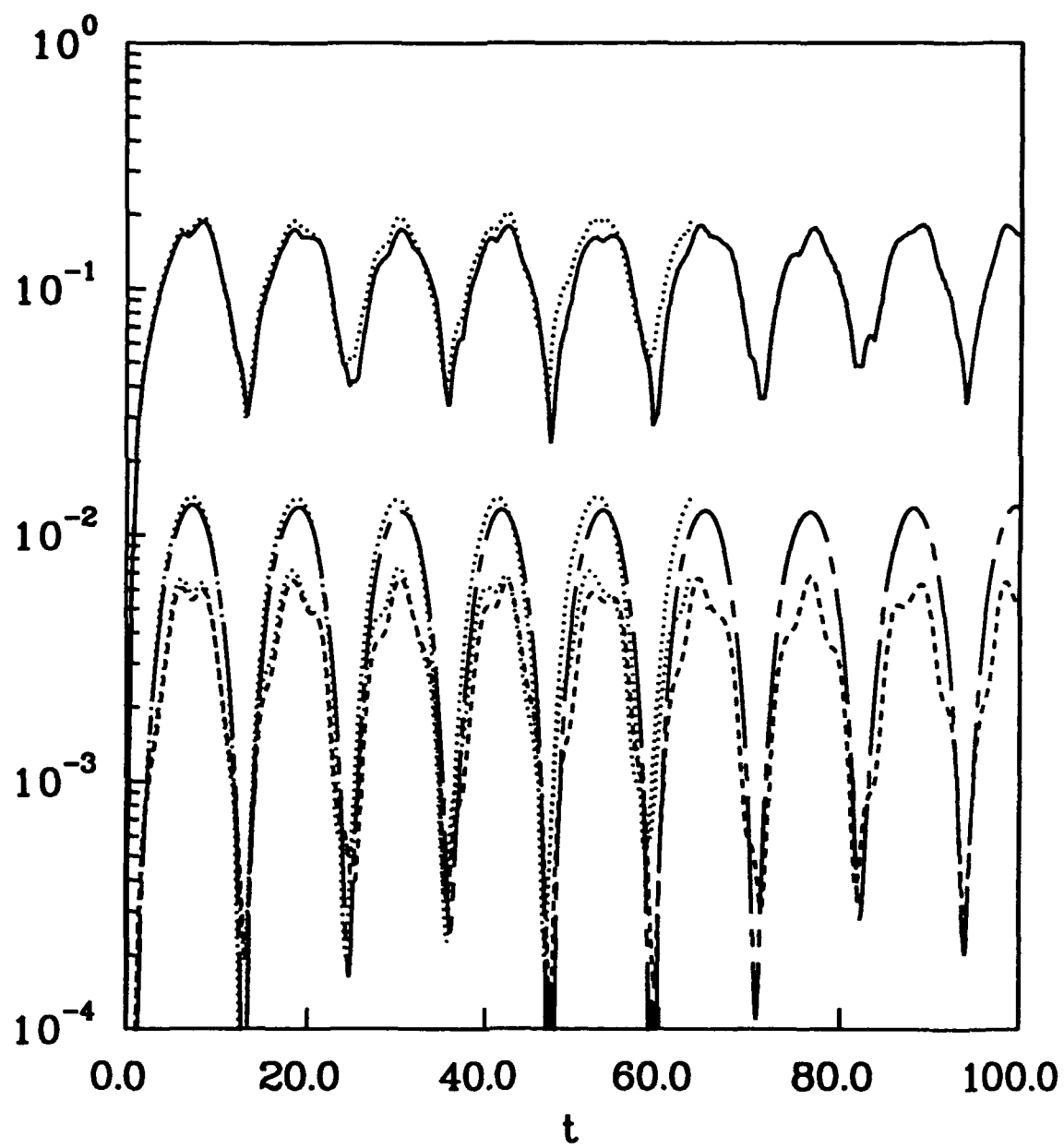


Fig. 10a

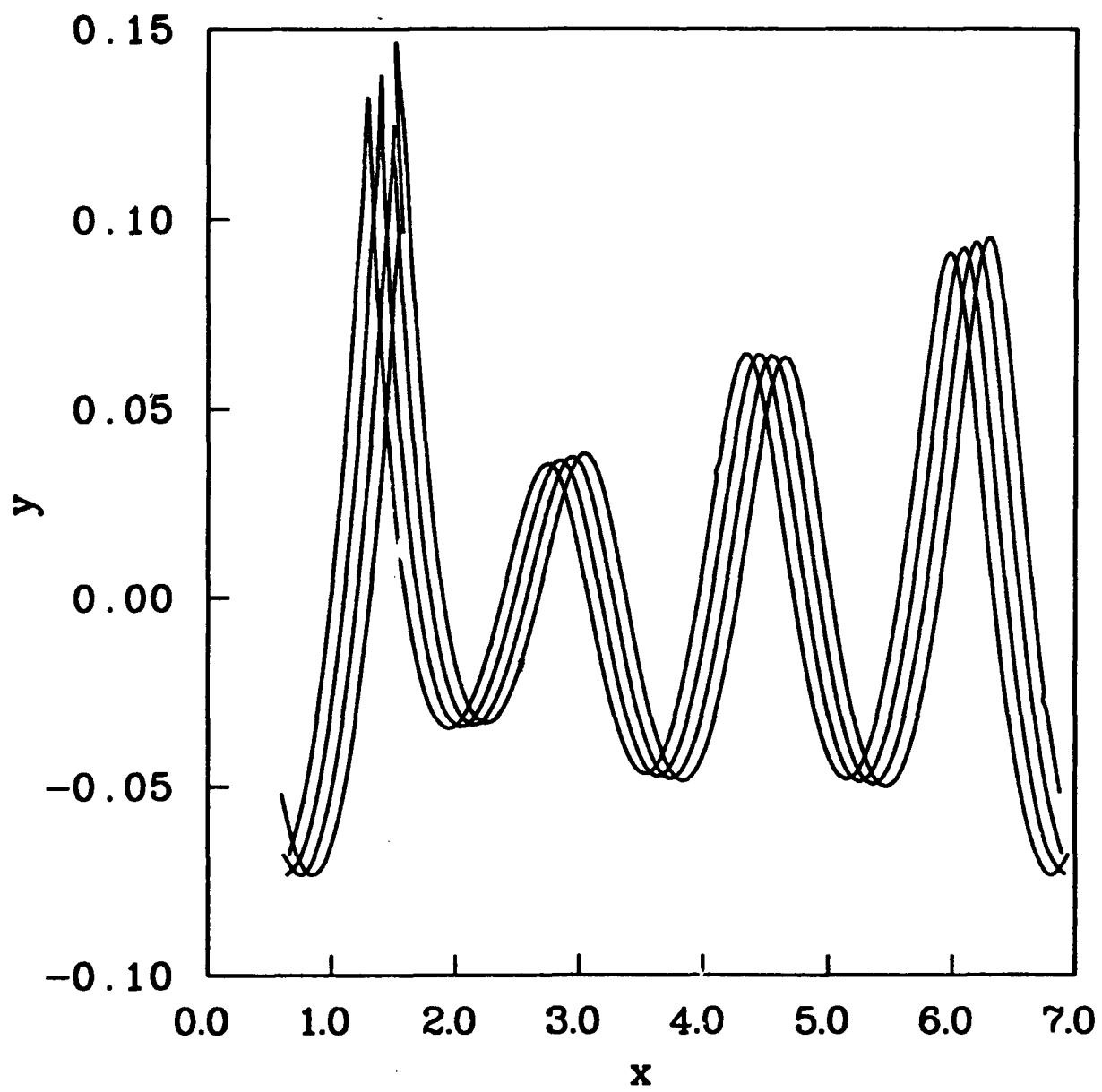


Fig. 10b

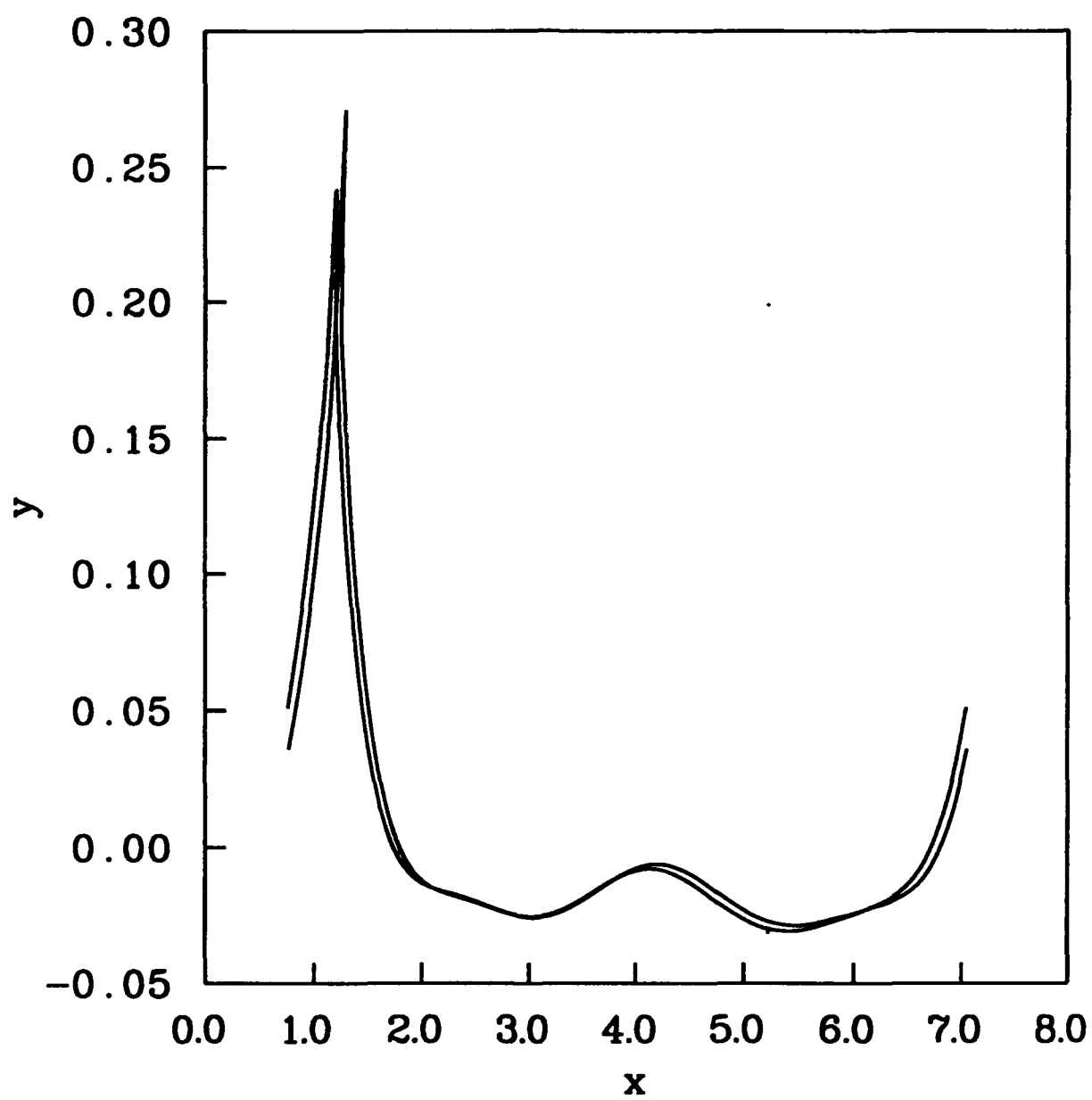


Fig. 11

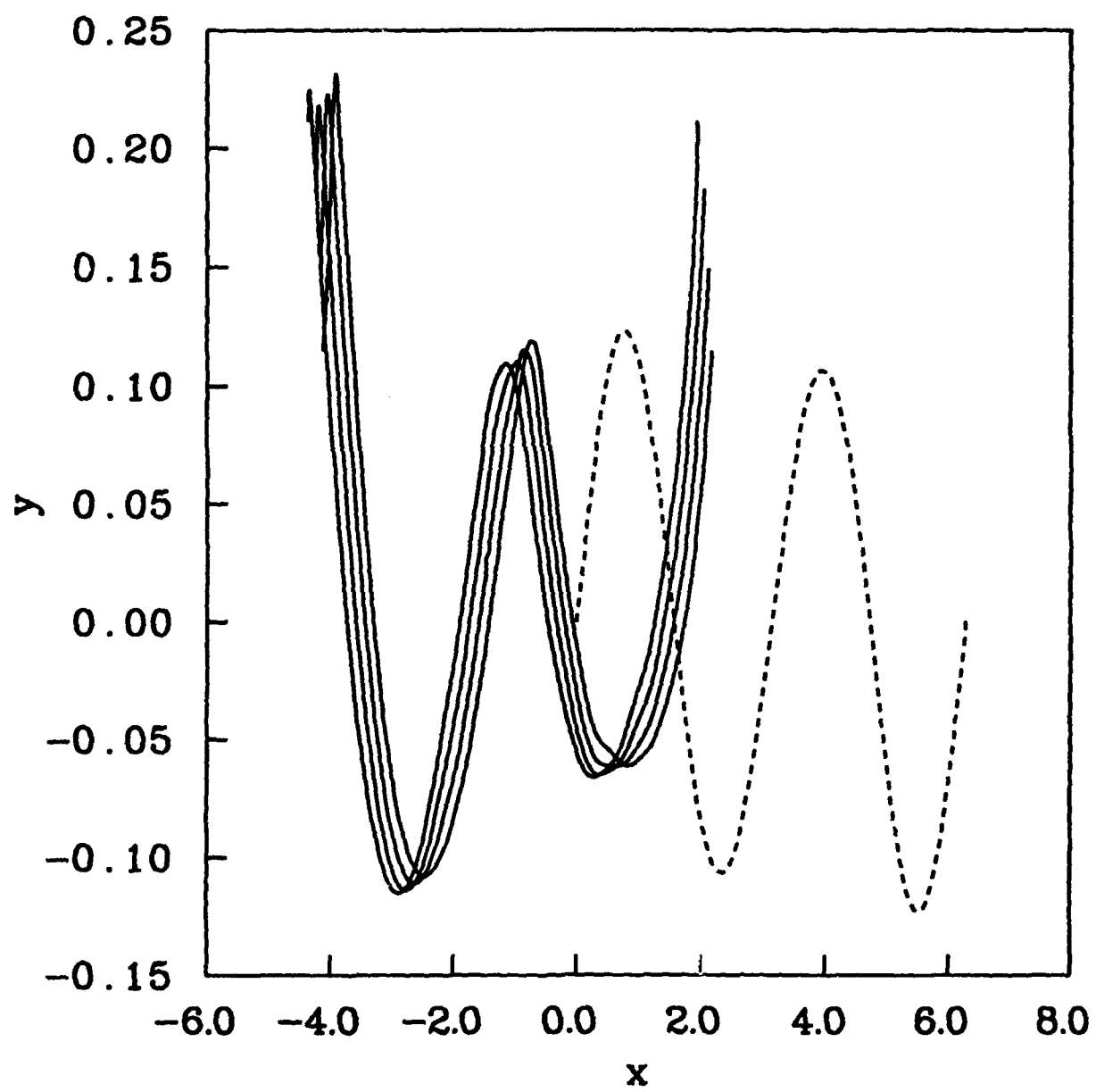


Fig. 12

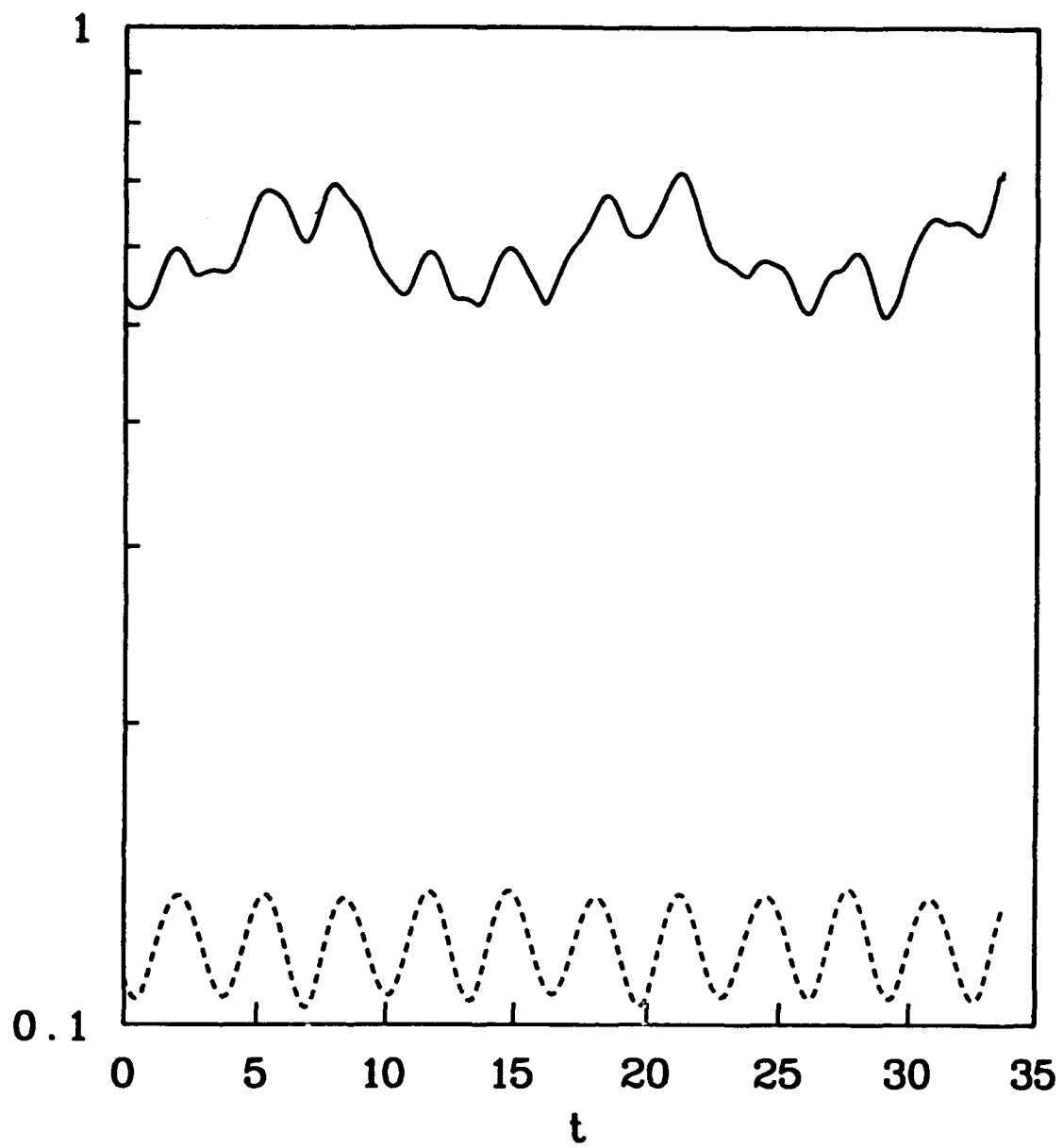


Fig 13

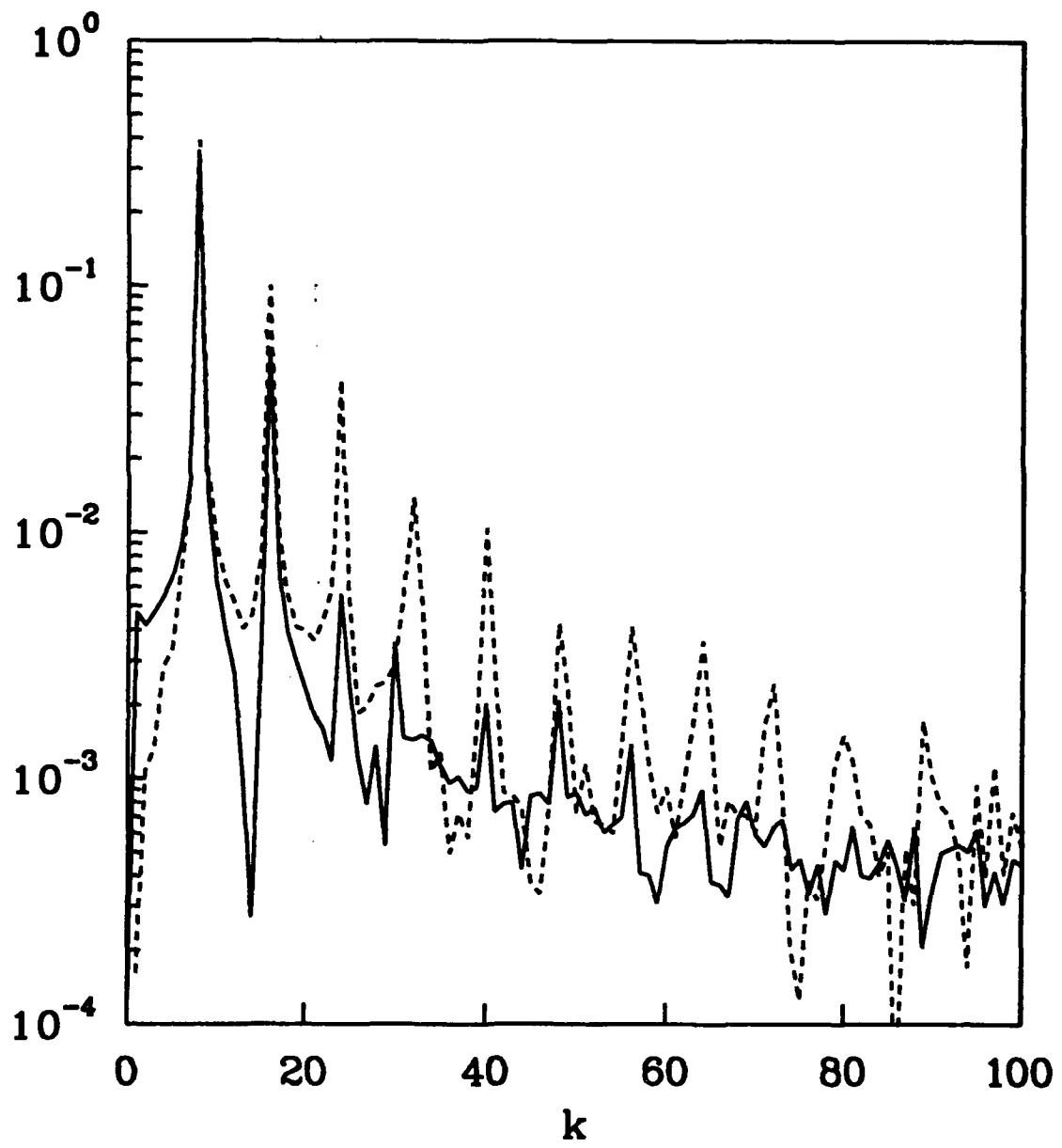


Fig. 14

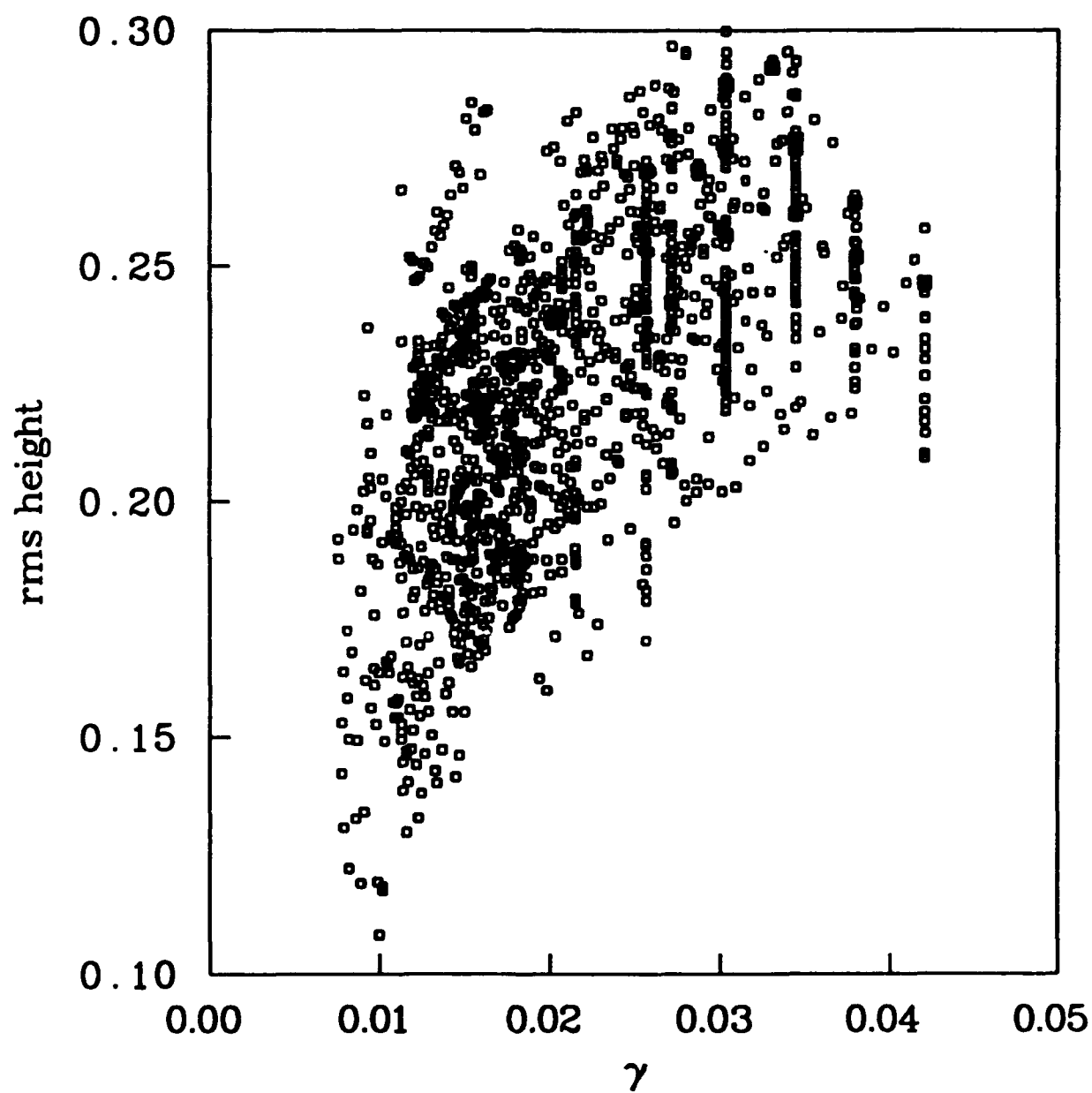


Fig. 15a

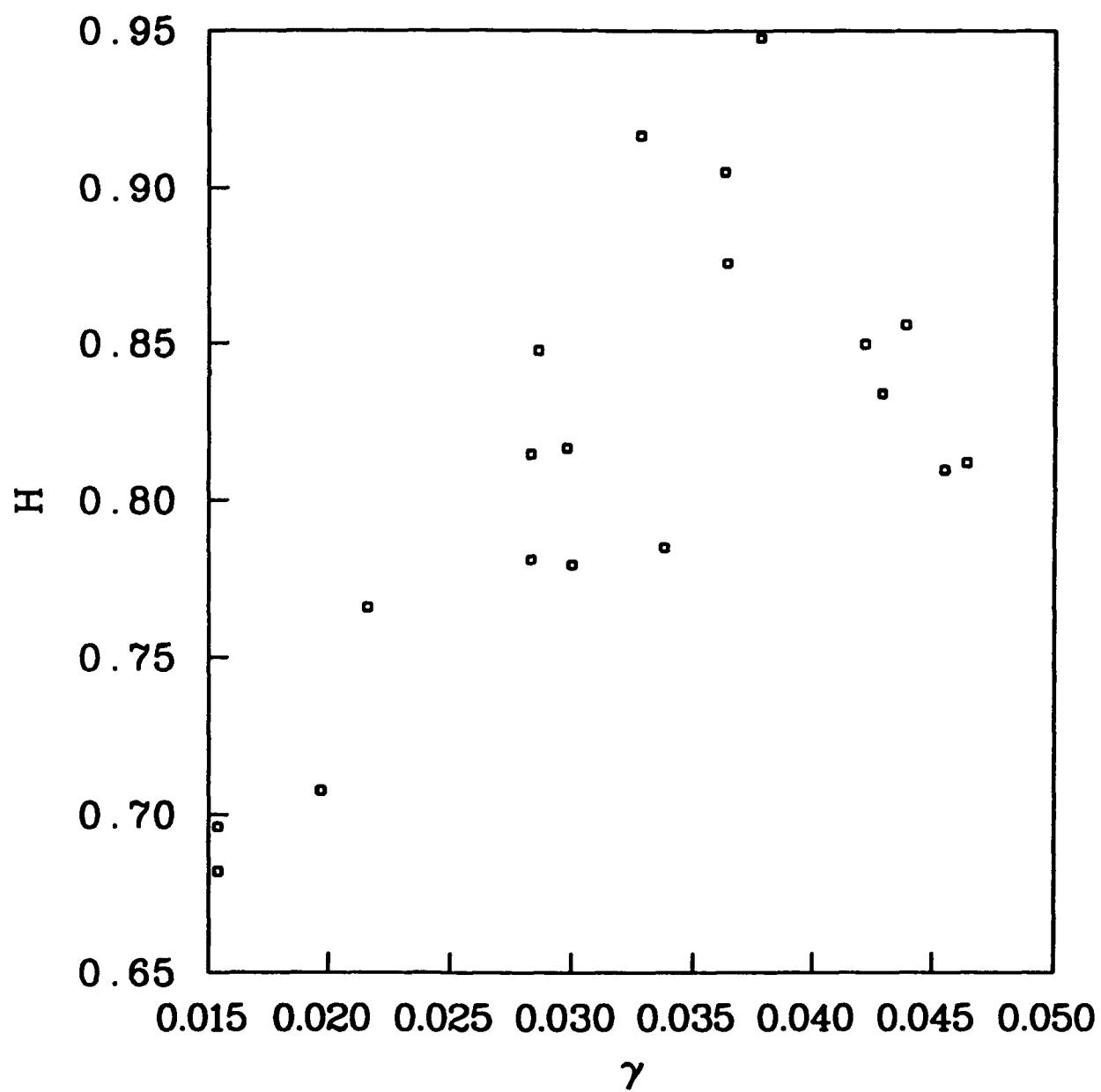


Fig. 15b

